#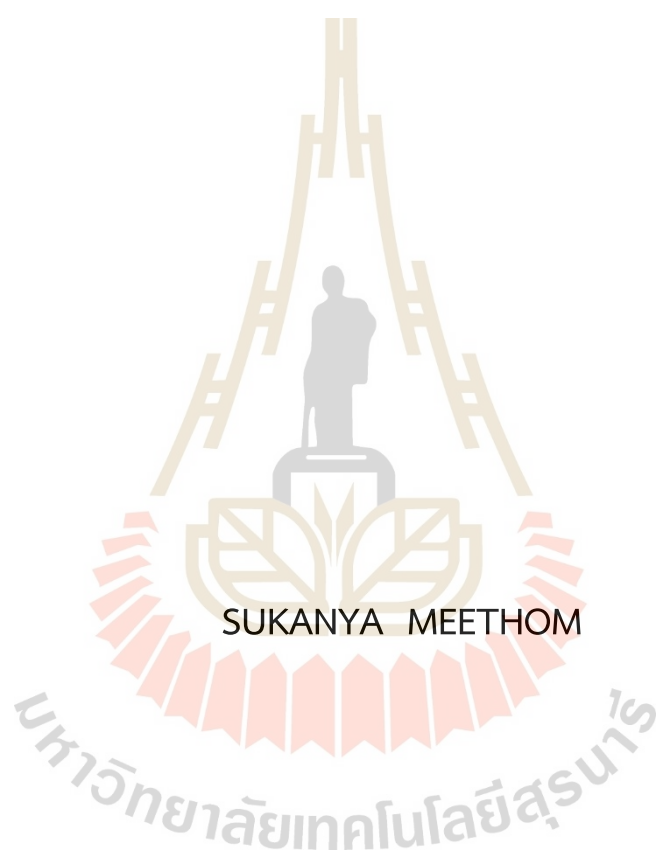 ENHANCED HYDROGEN SORPTION OF $LiBH_4$-$LiAlH_4$ BY QUENCHING DEHYDROGENATION, BALL MILLING, AND DOPING WITH MULTI-WALLED CARBON NANOTUBES

SUKANYA MEETHOM

A Thesis Submitted in Partial Fulfillment of the Requirements for the

Degree of Doctor of Philosophy in Chemistry

Suranaree University of Technology

Academic Year 2022

การเพิ่มประสิทธิภาพการดูดซับไฮโดรเจนของ $LiBH_4$–$LiAlH_4$ โดยหยุดการปลดปล่อยไฮโดรเจน การบด และการเติมมัลติวอลล์คาร์บอนนาโนทิวบ์

นางสาวสุกัญญา มีถม

ENHANCED HYDROGEN SORPTION OF $LiBH_4$-$LiAlH_4$ BY QUENCHING DEHYDROGENATION, BALL MILLING, AND DOPING WITH MULTI-WALLED CARBON NANOTUBES

Suranaree University of Technology has approved this thesis submitted in partial fulfillment of the requirements for the Degree of Doctor of Philosophy.

Thisis Examining Committee

_____

(Prof. Dr. Jatuporn Wittayakun)

Chairperson

_____

(Assoc. Prof. Dr. Rapee Utke)

Member (Thesis Advisor)

_____

(Dr. Narong Chanlek)

Member

_____

(Assoc. Prof. Dr. Sanchai Prayoonpokarach)

Member

_____

(Asst. Prof. Dr. Kamonwad Ngamchuea)

Member

_____   _____

(Assoc. Prof. Dr. Yupaporn Ruksakulpiwat)   (Prof. Dr. Santi Maensiri)

Vice Rector for Academic Affairs and   Dean of Institute of Science

Quality Assurance

สุกัญญา มีถม : การเพิ่มประสิทธิภาพการดูดซับไฮโดรเจนของ $LiBH_4$-$LiAlH_4$ โดยหยุดการปลดปล่อยไฮโดรเจน การบด และการเติมมัลติวอลล์คาร์บอนนาโนทิวบ์ (ENHANCED HYDROGEN SORPTION OF $LiBH_4$-$LiAlH_4$ BY QUENCHING DEHYDROGENATION, BALL MILLING, AND DOPING WITH MULTI-WALLED CARBON NANOTUBES) อาจารย์ที่ปรึกษา : รองศาสตราจารย์ ดร.ระพี อูทเคอ, 46 หน้า

กระบวนการผันกลับที่แย่ของ $LiBH_4$ และ $LiAlH_4$ (หรือ Li_3AlH_6) พบในสารประกอบ $LiBH_4$-$LiAlH_4$ เนื่องจากการจับตัวกันเป็นก้อนของ Al ในขณะการปลดปล่อยไฮโดรเจน ส่งผลให้การสร้าง AlB_2 และ LiAl ไม่มีประสิทธิภาพ กลยุทธ์ใหม่โดยการปลดปล่อยไฮโดรเจนทั้งหมดในขั้นตอนแรกของการปลดปล่อยไฮโดรเจนของ $LiBH_4$-$LiAlH_4$ ที่อุณหภูมิ 220 °C และการลดขนาดอนุภาคโดยการบด นำไปสู่การกระจายตัวที่ดีของทุกองค์ประกอบโดยเฉพาะ Al ถูกนำเสนอครั้งแรก นอกจากนี้ มัลติวอลล์คาร์บอนนาโนทิวบ์ถูกเติมในตัวอย่างที่ถูกบด เพื่อที่จะปรับปรุงการแพร่กระจายของไฮโดรเจน และการเหนี่ยวนำความร้อนซึ่งเป็นที่ชื่นชอบในการดูดซับไฮโดรเจนของไฮไดรด์สารประกอบ $LiBH_4$-$LiAlH_4$ แสดงให้เห็นการปลดปล่อยไฮโดรเจนที่แยกกันของ $LiAlH_4$ และ $LiBH_4$ เป็น LiH, Al, amorphous B, และ $Li_2B_{12}H_{12}$ นอกจากนี้ ในระหว่างการปล่อยไฮโดรเจนของตัวอย่างที่ถูกบดหลังทำให้ไฮโดรเจนหมดไปจะดำเนินการผ่านปฏิกิริยาของ Al กับ $LiBH_4$ และ LiH เพื่อสร้าง AlB_2 และ LiAl ตามลำดับ สิ่งนี้นำไปสู่จลนพลศาสตร์ที่เร็วขึ้น 3 เท่า การลดลงของอุณหภูมิที่เริ่มปล่อยไฮโดรเจนถึง 120 °C และการผันกลับได้ของ $LiBH_4$, $LiAlH_4$, และ Li_3AlH_6 สำหรับตัวอย่างที่เติมมัลติวอลล์คาร์บอนนาโนทิวบ์ แม้ว่า $LiAlH_4$ และ Li_3AlH_6 จะไม่สามารถเกิดการผันกลับได้ แต่จลนพลศาสตร์ได้ถูกปรับปรุงเนื่องจากอิทธิพลในทางบวกของมัลติวอลล์คาร์บอนนาโนทิวบ์

สาขาวิชาเคมี

ปีการศึกษา 2565

ลายมือชื่อนักศึกษา _สุกัญญา มีถม_

ลายมือชื่ออาจารย์ที่ปรึกษา _____

SUKANYA MEETHOM : ENHANCED HYDROGEN SORPTION OF LiBH$_4$-LiAlH$_4$ BY QUENCHING DEHYDROGENATION, BALL MILLING, AND DOPING WITH MULTI-WALLED CARBON NANOTUBES THESIS ADVISOR : ASSOC. PROF. RAPEE UTKE, Ph.D. 46 PP.

Poor reversibility of LiBH$_4$ and LiAlH$_4$ (or Li$_3$AlH$_6$) is found in LiBH$_4$-LiAlH$_4$ composites due to the agglomeration of Al upon dehydrogenation, resulting in the ineffective formation of AlB$_2$ and LiAl. A new strategy of quenching the first-step dehydrogenation of LiBH$_4$-LiAlH$_4$ composites at temperature of 220 °C and particle size reduction via ball milling, leading to good dispersion of all species especially Al, is proposed for the first time. Additionally, multiwalled carbon nanotubes (MWCNTs) are doped into the milled sample to enhance hydrogen diffusion and thermal conductivity, favoring hydrogen sorption of hydrides. The LiBH$_4$-LiAlH$_4$ composites show the individual decomposition of LiAlH$_4$ and LiBH$_4$ to LiH, Al, amorphous B, and Li$_2$B$_{12}$H$_{12}$. Moreover, decomposition of the milled sample quenched during dehydrogenation proceeds through reactions of Al with LiBH$_4$ and LiH to form AlB$_2$ and LiAl, respectively. This leads to three times faster kinetics, reduction of onset temperature by 120 °C, and reversibility of LiBH$_4$, LiAlH$_4$, and Li$_3$AlH$_6$. For the MWCNTs-doped sample, although LiAlH$_4$ and Li$_3$AlH$_6$ cannot be reproduced, kinetics is enhanced due to positive effects of MWCNTs.

School of Chemistry

Academic Year 2022

Student's Signature _____

Advisor's Signature _____

ACKNOWLEDGEMENTS

Sukanya Meethom

CONTENTS

CONTENTS (Continued)

LIST OF TABLES

LIST OF FIGURES

LIST OF FIGURES (Continued)

CHAPTER I

INTRODUCTION

1.1 Hydrogen Energy

Since last two centuries, energy consumption worldwide has mainly relied on fossil fuels, such as coal, crude oil, and natural gas. Via burning fossil fuels, especially in the combustion vehicles, air pollution due to the releases of CO_2, CO, SO_x, NO_x, etc. impacts detrimentally both environment and living quality. Moreover, the high energy consumption has resulted in the reduction of the crude oil supply, which is a critical obstacle for the future developments. For decades, renewable energy resources including solar, wind, geothermal, hydropower, biomass, and hydrogen have been of interest to replace fossil fuels. Since hydrogen offers many advantages of high energy density (142 MJ kg^{-1}) (Jain, I. P., Lal, and Jain, A., 2010), great varieties of sources (e.g., water, biomass, and organic matters (Figure 1.1)) and low environmental impact, usage of hydrogen in fuel cell for several applications of stationary powers, portable devices, and transportations has been widely proposed.
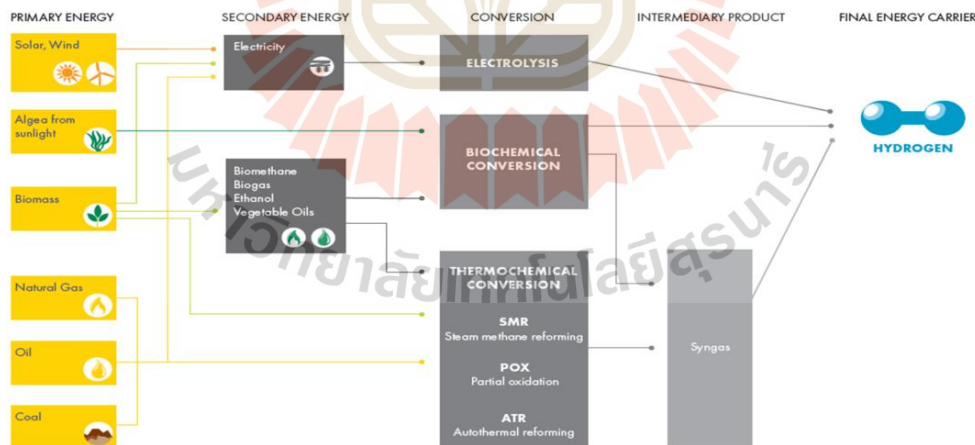
Figure 1.1 Processes of hydrogen productions (Shell Deutschland Oil GmbH 22284 Hamburg, 2017).

Hydrogen can be produced by steam methane reforming, partial oxidation, auto thermal reforming, or electrolysis methods, but the cost of these processes are quite high and they require energy in the production process. Therefore, scientists are turning to hydrogen production by biological methods or bio-hydrogen (Figure 1.2).
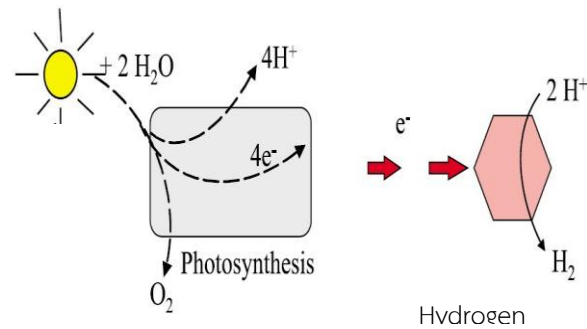
Figure 1.2 Bio-hydrogen processing cycle (Microbial Redox Metalloenzyme Research Group, 2005).

Figure 1.2 shows the bio-hydrogen processing cycle. This process is the production of hydrogen using solar energy. In this process, solar energy is captured by the photosynthetic apparatus, afterward, water is decomposed into oxygen (O_2), protons (H^+), and electrons (e^-). Electrons are delivered to hydrogenase enzyme to created hydrogen (Microbial Redox Metalloenzyme Research Group, 2005). The first commercial fuel cell vehicle (FCV) from Toyota, named Mirai was launched in Japan (2016) and planned to sale worldwide in the following years. In 2021, two hydrogen cars named Toyota Mirai and Hyundai Nexo have been released in selected markets (IHS Inc, 2016). Moreover, hydrogen fuel-cell vehicle name Honda Clarity was produced from 2016-2021 (Haymarket Media Group, 2021).
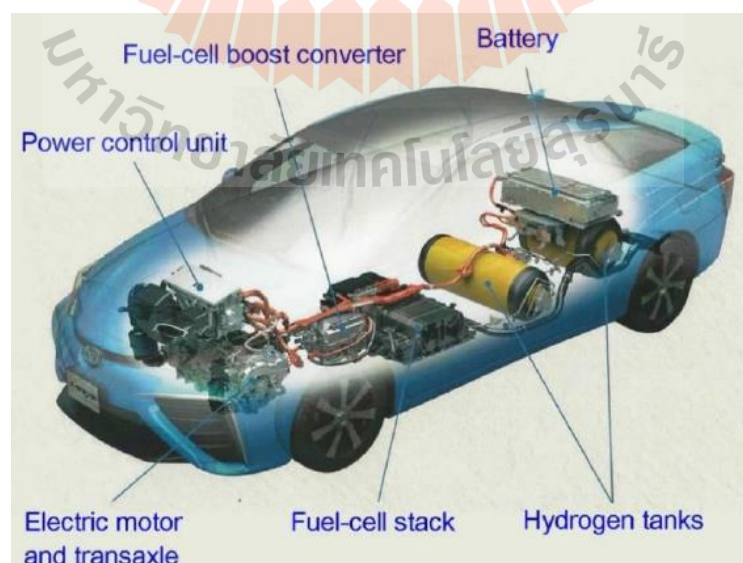
Figure 1.3 Components of Toyota Mirai (Tuan, Karpukhin, Terenchenko, and Kolbasov, 2018).

From Figure 1.3, the major components of Toyota Mirai are proton exchange membrane fuel cell (PEMFC) stack, compressed hydrogen storage tanks, nickel-metal hydride battery, power control unit, and motor. PEMFC stack consisting of 370 single cells (37.74 kg) provides maximum output of 114 kW (Yoshida and Kojima, 2015). For compressed hydrogen storage tank (p(H_2)= 70 MPa), volumetric and gravimetric hydrogen capacities are 40 gH_2/L and 5.7 wt. % H_2, respectively. Up to 5 kgH_2, required for 480 km driving distance can be filled in two compressed hydrogen gas tanks with total weight and volume of 87.5 kg and 122.4 L, respectively (Millikin, 2014).

1.2   Fuel Cells

There are several types of fuel cells, each of which is suited for different applications. Fuel cells are typically grouped according to their operating temperatures and types of electrolyte used (Table 1.1). The amount of power generated by a fuel cell is determined by several factors including fuel cell type, size, operating temperature, and pressure. The most common type of fuel cell used in FCVs is the polymer electrolyte membrane fuel cells (PEMFCs).
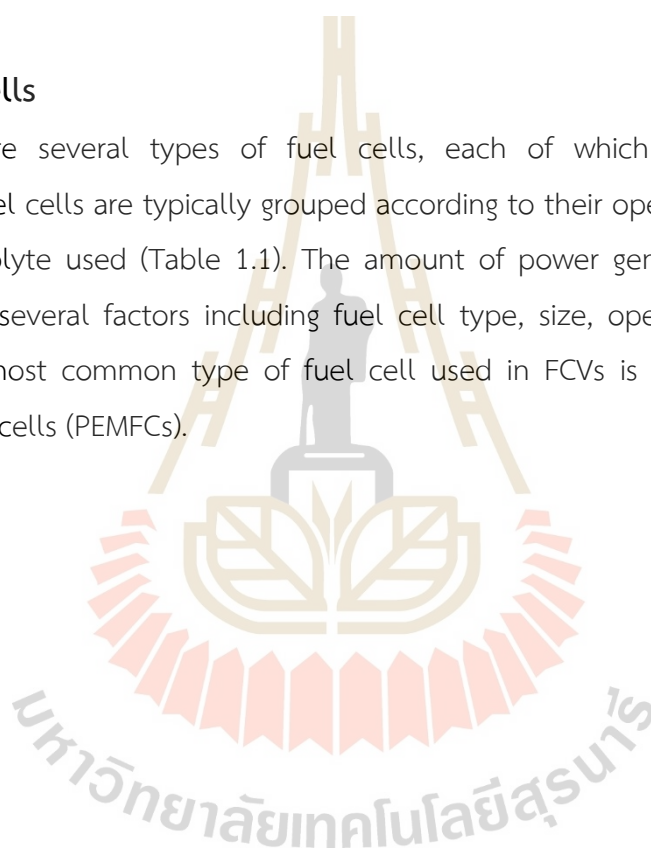
Table 1.1 Types of fuel cells (Larminie, 2003; U.S. Department of Energy, 2023).

Fuel cell types	Electrolytes	Operating temperature (°C)	Applications
Proton exchange membrane fuel cells (PEMFCs)	Polymers	50-90	- Transportation - Specialty vehicles - Portable power - Backup power - Distributed generation
Alkaline fuel cell (AFC)	Solution of KOH in water	60-90	- Transportation - Military - Submarine - Backup power
Direct methanol fuel cells (DMFCs)	CH_3OH/CO_2	80-110	- Portable power - Vehicles - Military - Man-portable tactical equipment
Phosphoric acid (PAFC)	H_3PO_4	160-220	- Distributed generation
Molten carbonate fuel cell (MCFC)	molten Na_2CO_3	600-700	- Military - Electrical utility - Power plants
Solid oxide fuel cell (SOFC)	ZrO_2	700-1,000	- Auxiliary power - Electric utility - Distributed generation
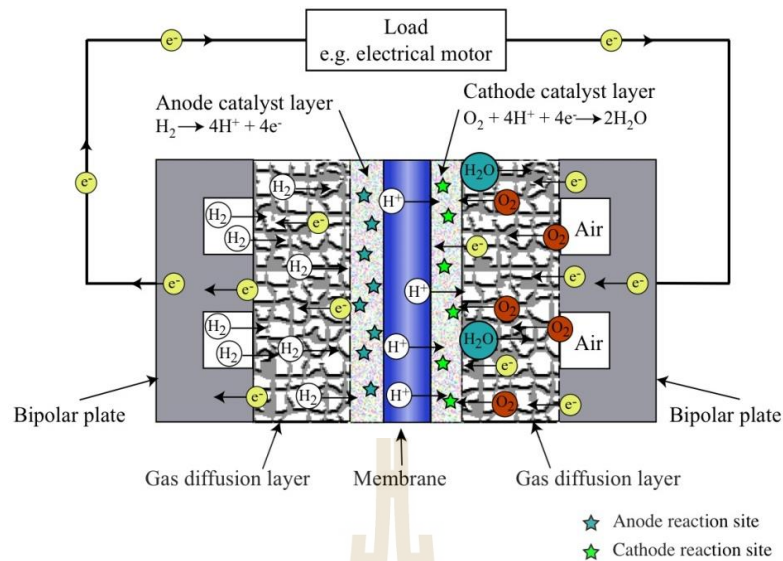
Figure 1.4 Polymer electrolyte membrane fuel cells (PEMFCs).

(http://www.mece.ualberta.ca/groups/energysystemsdesign/research.html)

PEMFCs consist of polymer electrolyte membrane (PEM), electrodes, bipolar plates, and gas diffusion layers (Figure 1.4). The PEM placed between anode (negative electrode) and cathode (positive electrode) by pressure/temperature compression is denoted as a membrane electrode assembly (MEA). Hydrogen gas supplied to anode performs oxidation reaction (equation (1.1)) to produce protons (H^+) and electrons (e^-).

$$2H_2 \quad \rightarrow \quad 4H^+ + 4e^- \tag{1.1}$$

The PEM allows only protons passing through to cathode, while the electrons travel through an external circuit to the anode. The flow of electrons through this circuit creates the electric current. At cathode, oxygen gas reacts with protons and electrons to produce water and heat (equation (1.2)). Overall redox reaction of PEMFC is shown in equation (1.3).

$$O_2 + 4H^+ + 4e^- \quad \rightarrow \quad 2H_2O + \text{Heat} \tag{1.2}$$

$$2H_2 + O_2 \quad \rightarrow \quad 2H_2O + \text{Heat} \tag{1.3}$$

Although redox reaction rate in PEMFCs can be improved by increasing operating temperature (> 100 °C), evaporation of water molecules acting as proton carriers in PEM (e.g., Nafion membrane) results in significant reduction of proton conductivity. Therefore,

research and developments on the enhancement of operating temperature of PEM by preparation of polymer-inorganic composites and syntheses of thermally stable polymers have been intensively focused. Besides operating temperature, purity of hydrogen gas supplied to PEMFC is another concern. For example, carbon monoxide (CO) impurity in hydrogen gas produced from steam natural gas reforming process can seriously poison the platinum (Pt) catalyst at electrodes. The other factor affecting the performance of on-board PEMFCs in transportation is hydrogen storage systems with high hydrogen capacity, operating at moderate temperature and pressure condition, fast hydrogen charging and discharging, and low cost.

Table 1.2 Competing technologies for hydrogen storage systems (Varin, Czujko, and Wronski, 2009; Hirscher, 2009).

Storage systems	Volumetric hydrogen capacity (kgH_2 m^{-3})	Drawbacks
Compressed hydrogen gas under 80 MPa pressure	~40	-Safety problem -Cost of pressurization -Large pressure drop during use hydrogen
Liquefied hydrogen at cryogenic temperature (-252 °C or 21 K)	~71	-Large thermal losses -Safety -Cost of liquefaction
Cryo-compressed hydrogen (350 bar, 63 K)	~80	-Large thermal losses -Safety problem
Solid state hydrides	80-160	-High hydrogen desorption/ absorption temperature -Slow hydrogen desorption/ absorption kinetics -Release of toxic gases during operation (e.g., B_2H_6 from decomposition of $LiBH_4$

Considering compressed hydrogen gas system used in the car (Toyota Mirai, Figure 1.3), not only materials and technology for tank fabrication are expensive to resist high hydrogen pressure (80 MPa) and impact in the case of accident, but also cost of pressurization. Moreover, low storage capacity (40 kgH$_2$ m^{-3}) is obtained despite compression under high pressure. For liquefied hydrogen, although hydrogen can be stored at lower pressure than compressed hydrogen system, remarkable cost of insulation for storage tank and refilling station to keep hydrogen in liquid form (at 20 K) hampers its use in practical application. Thus, further development of cryo-compressed system has been proposed. In this system, hydrogen can be stored in the form of liquid-gas mixture at higher temperature than liquefied hydrogen (63 K) and lower pressure than compressed gas (35 MPa). In addition, cryo-compressed system provides superior hydrogen storage capacity (80 kgH$_2$ m^{-3}) to compressed and liquefied hydrogen. However, hydrogen stores at nearly cryogenic temperature and high pressure in cryo-compressed system, therefore, hydrogen storage tank with good thermal insulation and high pressure tolerance cannot be avoided. In the case of solid state hydrides, high theoretical volumetric and gravimetric capacities of 80-160 kgH$_2$ m^{-3} and 5-18 wt. %, respectively (Züttel, Remhof, Borgschulte, and Friedrichs, 2010) are attractive for hydrogen storage applications. However, hydride materials still have some obstacles based on severe temperature and pressure conditions for hydrogen desorption/absorption (e.g., above 400 °C and 600 °C (under 35 MPa H$_2$) (Orimoa, Nakamoria, and Kitaharaa, 2005) for hydrogen desorption and absorption, respectively, for LiBH$_4$), slow hydrogen desorption/absorption kinetics (rehydrogenation of LiBH$_4$ at ~600 °C, 35 MPa H$_2$, for >12 h) (Züttel, Wenger, and Rentsch, 2003), and release of toxic gases during operation (e.g., B$_2$H$_6$ from LiBH$_4$). With respect to the targets of hydrogen storage system for fuel cell vehicles (Table 1.3), in this wok we aim to improve the performances of hydride materials focusing on high hydrogen content released and reproduced, fast hydrogen exchange reaction rate, and low temperature and pressure for de/rehydrogenation.

Table 1.3 US DOE Freedom CAR hydrogen storage system targets (U.S. Department of Energy, 2023).

Targeted factors	2020	2025	Ultimate
Compressed automotive hydrogen storage systems			
Gravimetric density			
kWh/kg system	1.5	1.8	2.2
(kg H_2/kg system)	(0.045)	(0.055)	(0.065)
Volumetric density			
kWh/L system	1.0	1.3	1.7
(kg H_2/L system)	(0.030)	(0.040)	(0.050)
Cost			
$/kWh	10	9	8
($/kg H_2)	(333)	(300)	(226)
Durability/Operability			
Operating ambient temperature (°C)	-40/60	-40/60	-40/60
Min/max delivery temperature from storage system (°C)	-40/85	-40/85	-40/85
Operational cycle life (1/4 tank to full) (cycles)	1,500	1,500	1,500
Min/max delivery pressure from storage system (bar)	5/12	5/12	5/12
System fill time (min)	3-5	3-5	3-5

1.3   References

Haymarket Media Group. Honda discontinues hydrogen-fuelled Clarity FCV due to slow sales (June 16, 2021). Retrieved May 29, 2023, from Wikipedia: https://en.wikipedia.org/wiki/Hydrogen_vehicle

Hirscher, M. (2009). *Handbook of hydrogen storage: New materials for future energy storage.* Germany: Betz-druck GmbH, Darmstadt.

IHS Inc. Global hydrogen fuel cell electric vehicle market buoyed as OEMs will launch 17 vehicle models by 202, IHS Says. (May 4, 2016). Retrieved May 29, 2023, from Wikipedia: https://en.wikipedia.org/wiki/Hydrogen_vehicle

Jain, I. P., Lal, C., and Jain, A. (2010). Hydrogen storage in Mg: A most promising material. *Int. J. Hydrogen Energy.*, *35*, 5133-5144.

Larminie, J. (2003). *Fuel cell systems explained*. England: John Wiley & Sons.

Microbial Redox Metalloenzyme Research Group (2005). *Hydrogenase.* Retrieved from http://biotech.szbk.u-szeged.hu/h2ase.html.

Millikin, M. (2014). *Toyota FCV Mirai launches in LA. Initial TFCS specs; $57,500 or $499 lease; leaning on Prius analogy.* Retrieved from http://www.greencarcongress.com/2014/11/20141118-mirai.html

Orimoa, S., Nakamoria, Y., and Kitaharaa, G. (2005). Dehydriding and rehydriding reactions of LiBH$_4$. *J. Alloys Compd.*, *404-406,* 427-430.

Shell Deutschland Oil GmbH 22284 Hamburg. (2017). *Shell hydrogen study energy of the future? Sustainable mobility through fuel cells and H$_2$.* Retrieved from www.shell.de/h2study and www.shell.com/hydrogen

Tuan, N. K., Karpukhin, E. K., Terenchenko, A. S., and Kolbasov, A. F. (2018). World trends in the development of vehicles with alternative energy sources. *J. Eng. Appl. Sci., 13*(7), 2535-2542.

U.S. Department of Energy. (2023). *DOE Technical Targets for Onboard Hydrogen Storage for Light-Duty Vehicles.* Retrieved from http://www.energy.gov/eere/fuelcells/doe-technical-targets-onboard hydrogen-storage-light-duty-vehicles

Varin, R. A., Czujko, T., and Wronski, Z. S. (2009). Nanomaterials for solid state hydrogen storage. Springer Science and Business Media. ISBN 978-0-387-77711-5.

Yoshida, T., and Kojima, K. (2015). Toyota MIRAI fuel cell vehicle and progress toward a future hydrogen society. *Electrochem. Soc. Interface.,* 45-49.

Züttel, A., Remhof, A., Borgschulte, A., and Friedrichs, O. (2010). Hydrogen: the future energy carrier. *Philos. Trans. A. Math. Phys. Eng. Sci.*, *368*(1923), 3329-3342.

Züttel, A., Wenger P., and Rentsch, S. (2003). LiBH$_4$ a new hydrogen storage material. *J. Power Sources., 118*, 1-7.

CHAPTER II
LITERATURE REVIEWS

Among all hydrogen storage systems, solid state hydrides are the most favorable system in transportation applications, as shown in the comparison in Table 1.2. Therefore, several research groups have attempted to develop these materials for future utilization. There are several metal hydrides, complex hydrides, and composite hydrides, for example, ammonia borane (NH_3BH_3) and its derivatives (Silvearv, 2011; Sutton et al., 2011; Xiong et al., 2007; Guo, Wu, Zhou, and Yu, 2011) metal aluminium hydrides (e.g., $NaAlH_4$, Na_3AlH_6, Na_2LiAlH_6) (Bogdanovic, and Schwickardi, 1997; Sun, Srinivasan, Kiyobayashi, Kuriyama, and Jensen, 2003; Fu, Ramirez-Cuesta, and Tsang, 2006) and metal borohydrides ($Ca(BH_4)_2$, $LiBH_4$) (Rongeata et al., 2010; Gross, Vajo, Van Atta, and Olson, 2008). Various hydrogen storage options for mobile applications are shown in Figure 2.1. There are hydrogen adsorptions on solids of large surface area, hydrogen storage by metal hydrides, alanates and other light hydrides, etc.

Figure 2.1 Volumetric versus gravimetric hydrogen density of various hydrogen storage systems (Züttel, Remhof, Borgschulte, and Friedrichs, 2010).

From Figure 2.1, each material or system owns specific gravimetric and volumetric densities in the ranges of 2-25 wt. % and 20-150 kgH_2/m^{-3}, respectively. Some of them have high gravimetric density with low volumetric value (compressed hydrogen gas) and vice versa (e.g., intermetallic hydrides of $BaReH_9$ and $LaNi_5H_6$). Materials or systems with high volumetric and gravimetric densities benefit compact size and light weight for hydrogen

storage tank. Thus, the most desirable materials or systems should be located in the upper right corner of the plot, for example, hydrogen chemisorbed on carbon and lithiumborohydride ($LiBH_4$). Although $LiBH_4$ has high theoretical gravimetric and volumetric hydrogen densities of 18.5 wt. % and 121 kg H_2/m^3, respectively (Li, Peng, Zhou, and Wan, 2011), it starts to liberate hydrogen at temperature above 380 °C and only half of hydrogen content can be obtained below 600 °C (Züttel et al., 2003). Considering the pressure-concentration-temperature (PCT) isotherm measurements (T= 410-520 °C), the enthalpy (ΔH) and entropy (ΔS) for dehydrogenation of $LiBH_4$ were 74 kJ/mol H_2 and 115 J/K mol H_2, respectively (Mauron, Buchter, and Friedrichs, 2008). In addition, dehydrogenation products of $LiBH_4$ (LiH and B) according to equation (2.1) can be reversible under severe condition of T= 600 °C and $p(H_2)$= 35 MPa (Orimoa et al., 2005).

$$LiBH_4(l) \quad \rightarrow \quad LiH(s) + B(s) + 3/2H_2(g) \qquad (2.1)$$
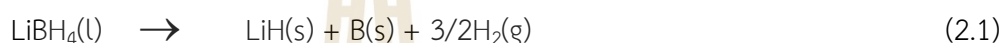
These de/rehydrogenation conditions of $LiBH_4$ are too high to meet the requirements for fuel cell operation. Therefore, several approaches, such as doping with catalysts and/or additives, nanoconfinement in porous materials, and reactive hydride composites (RHCs) have been considered to solve these problems.

2.1   Doping with catalysts and/or additives

The effects of other additives, such as TiO_2, $TiCl_3$, TiF_3, $MgCl_2$, and NbF_5 (Au, Jurgensen, and Zeigler, 2006; Guo et al., 2009; Au, Spencer. Jurgensen, and Zeigler, 2008; Kou et al., 2014) on de/rehydrogenation of $LiBH_4$ have been investigated. For example, $LiBH_4$ + $0.3TiO_2$, desorbed 9 wt. % H_2 in the temperature range of 100-600 °C and absorbed 8 wt. % H_2 at 600 °C under 7 MPa H_2. The composites of $LiBH_4$ + $0.2MgCl_2$ + $0.1TiCl_3$ revealed onset dehydrogenation temperature at 60 °C and desorbed 5 wt. % H_2 at 400 °C. Reversibility of $LiBH_4$ in $LiBH_4$ + $0.2MgCl_2$ + $0.1TiCl_3$ composites (4.5 wt. % H_2) could be accomplished at 600 °C under 7 MPa H_2 (Au et al., 2006, 2008). In the case of $3LiBH_4$-TiF_3, 5 wt. % H_2 was obtained in the temperature range of 100 to 250 °C and 4 wt. % H_2 could be reversible at 350 °C under 10 MPa H_2. Afterward, Kou et al. (2014) proposed $xLiBH_4$-NbF_5 mixtures (x = 1, 5, 10, 20, 40) and found that $5LiBH_4$-NbF_5 sample performed the best results, i.e., onset dehydrogenation temperature reduced to 60 °C together with 4 wt. % H_2 below 255 °C (Figure 2.2). During dehydrogenation, unidentified intermediate was formed and decomposed to NbB_2 and LiF. The formation of NbB_2 destabilized $LiBH_4$ and reducing dehydrogenation temperature. However, $5LiBH_4$-NbF_5 revealed poor reversibility (only 0.5 wt. % H_2) since dehydrogenation process was exothermic.
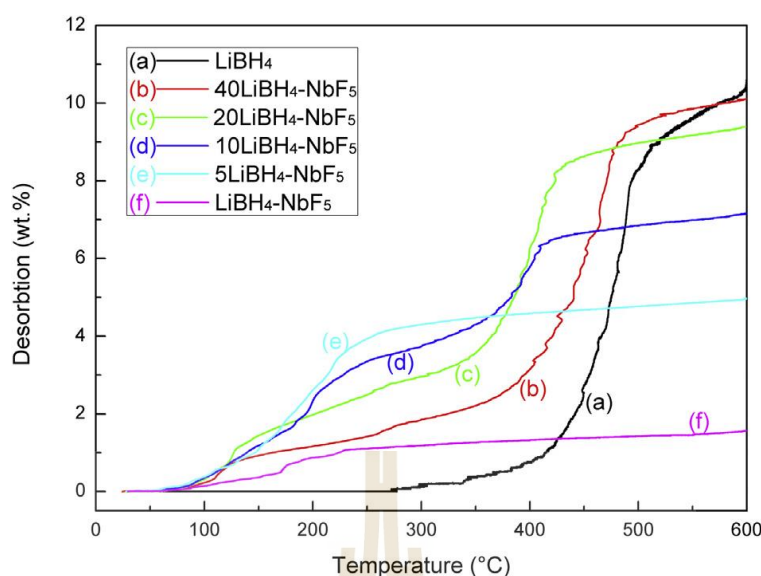
Figure 2.2 Temperature-programmed dehydrogenation (TPD) curves of $xLiBH_4-NbF_5$ mixtures (x = 1, 5, 10, 20, 40) and pristine $LiBH_4$ (Kou et al., 2014).

Besides transition metal based additives, doping with carbon materials into $LiBH_4$ have been widely carried out. For example, Fang et al. (2010) milled $LiBH_4$ with 30 wt. % of various carbon additives, such as graphite (G), purified single-walled carbon nanotubes (SWNTs), and activated carbon (AC). Reduction of onset dehydrogenation temperature and improvement of dehydrogenation kinetics were observed from all samples. The best performance was shown in $LiBH_4$-30 wt. % SWCNT (onset dehydrogenation at 190 °C together with 5 wt. % H_2 below 400 °C). In this regard, SWNTs might provide more nucleation sites for decomposition of $LiBH_4$ and favorable confined environment than G and AC. However, agglomeration of $LiBH_4$ was observed after rehydrogenation. Moreover, Zhu et al. (2015) proposed $LiBH_4$/graphene and $LiBH_4$/graphene-10 wt. % CeF_3. By doping with graphene into $LiBH_4$, de/rehydrogenation kinetics improved significantly with respect to bulk $LiBH_4$ (6 wt. % H_2 released at 425 °C within 3 h) and further development on kinetic property could be obtained by doping with 10 wt. % CeF_3 into $LiBH_4$/graphene (6.44 wt. % H_2 released at 425 °C within 1.30 h). The latter could be due to the formation of CeB_6, destabilizing $LiBH_4$ as in case of NbB_2 formed during dehydrogenation of $LiBH_4$-NbF_5 composites (Kou et al., 2014). However, CeB_6 showed no reversibility to form $LiBH_4$ after rehydrogenation at 440 °C under 3.3 MPa for 11 h. This resulted in only 6.14 wt. % H_2 was reproduced from $LiBH_4$/graphene-10 wt. % CeF_3, while of $LiBH_4$/graphene was 7.40 wt. % H_2. Therefore, it could be concluded that graphene played a major role in enhancing reversibility. Afterward, Wang et al. (2016) reported the effects of nanostructured graphite (NG) on hydrogen storage properties of $LiBH_4$.
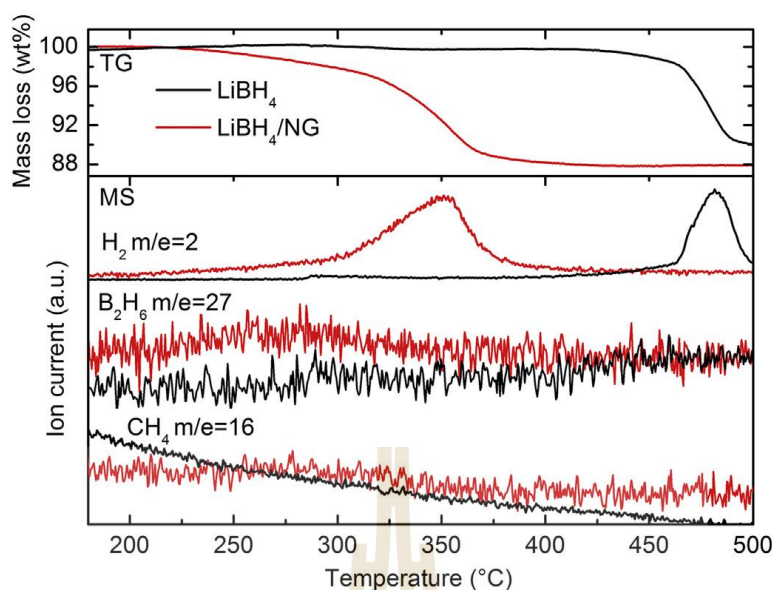
Figure 2.3 TG/MS profiles of the pure $LiBH_4$ (black) and $LiBH_4$/NG composites (red). The ramping rate is 5 °C/min (Wang, Kang, Ren, and Wang, 2016).

After doping with NG, onset and main dehydrogenation temperatures of $LiBH_4$ reduced from 400 to 300 °C and 475 to 350 °C, respectively, together with 12 wt. % H_2. However, $LiBH_4$/NG released small amount of B_2H_6 at low temperature of 275 °C (Figure 2.3). These could be due to the fact that graphite fragments were occupied by BH_3 complexes and H atoms from $LiBH_4$, yielding the reduction of dehydrogenation temperature of $LiBH_4$ but might produce B_2H_6 (Zhang, Ding, Liu, Zhang, and Huang, 2013). After rehydrogenation at 350 °C under 10 MPa H_2 for 10 h, $LiBH_4$/NG reproduced 6.3 and 4.7 wt. % during the 2nd and 3[td] cycles, respectively. Deficient hydrogen capacity with respect to the 1st cycle could be the formation of Li_3BO_3 after rehydrogenation. Moreover, composites of $LiBH_4$ with metallic aluminium (Al) (Ravnsbæk, and Jensen, 2012) and Al-containing compounds (e.g., AlH_3, $LiAlH_4$ and Li_3AlH_6) (Liu et al., 2016; Mao, Guo, Liu, Yu, 2009; Wu et al., 2012; Natthaporn Thaweelap and Rapee Utke, 2016) have been intensively investigated. Kang et al. (2007) modified $LiBH_4$ by ball-milling with Al. During cycling, AlB_2 was formed in the dehydrogenated state and disappeared in the hydrogenated state according to equation (2.2).

$$LiBH_4(s) + 1/2Al(s) \longrightarrow LiH(s) + 1/2AlB_2(s) + 3/2H_2(g) \qquad (2.2)$$

The formation of AlB_2 destabilized $LiBH_4$, resulting in the reduction of dehydrogenation enthalpy (from 74 to 18.8 kJ mol^{-1} H_2) and enhancement of dehydrogenation kinetics (7.2 wt. % H_2 released at 450 °C within 3 h). The $LiBH_4$-1.5Al desorbed hydrogen via several reaction steps through unknown intermediates and produced LiAl and $Li_{1-x}Al_xB_2$,

encouraging reversibility of $LiBH_4$ upon rehydrogenation (T= 400 °C and p(H_2)= 100 bar). Nevertheless, the other composites with lower Al content ($LiBH_4$-0.5Al) accomplished full dehydrogenation to form LiAl and $Li_{1-x}Al_xB_2$ only after doping with 2 mol % TiB_2. Besides, amorphous B detected after dehydrogenation due to deficient Al content led to incomplete rehydrogenation (Ravnsbæk, and Jensen, 2012). Theoretical calculation of $LiBH_4$-Al system exhibited Al replacement at Li and B atoms and occupation in interstitial sites of $LiBH_4$ (Weiqing, and Shilong, 2017). This led to weaker B-H bonding interaction and formation of Al-B bond, favoring hydrogen desorption.

2.2   Reactive Hydride Composites (RHCs)

A typical example for destabilization of $LiBH_4$ is the reactive hydride composites of $2LiBH_4$-MgH_2. Vajo et al. (2005, 2007a, 2007b) reported the enhanced hydrogen sorption properties of $LiBH_4$ composting with MgH_2. The formation of MgB_2 upon dehydrogenation reduced de-/rehydrogenation enthalpy from 67 (T= 410 °C) to 46 kJ/mol H_2 (Figure 2.4).

Bösenberg et al. (2007) proposed the reaction mechanism of $2LiBH_4$-MgH_2 composites as the following reaction:

$$2LiBH_4(s) + MgH_2(s) \longrightarrow 2LiH(s) + MgB_2(s) + 4H_2(g) \quad (11.6 \text{ wt. \%}) \qquad (2.3)$$
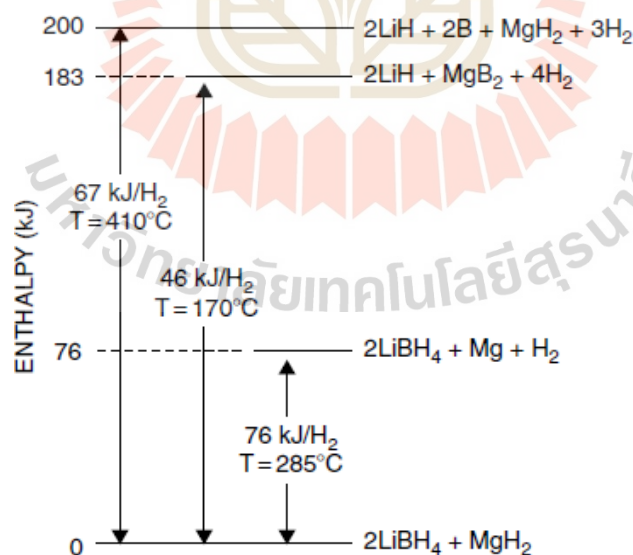
Figure 2.4 Enthalpy diagram revealing the destabilization of $LiBH_4$ by compositing with MgH_2 (Vajo and Olson, 2007).

Shim et al. (2009) studied the effects of back pressure on dehydrogenation of $LiBH_4$-based reactive hydride composites (e.g., $LiBH_4$ + YH_3, $6LiBH_4$ + CeH_2, and $6LiBH_4$ + CaH_2). They found that hydrogen back pressure promotes the formation of metal borides (e.g.,

YB_4, CeB_6, and CaB_6) during dehydrogenation. This attributed to the improvement of dehydrogenation kinetics (Figure 2.5). Dehydrogenation reactions of the mentioned composites are revealed in the following reactions:

$$4LiBH_4(s) + YH_3(s) \quad \longrightarrow \quad 4LiH(s) + YB_4(s) + 7.5H_2(g) \quad (8.5 \text{ wt. \%}) \quad (2.4)$$

$$6LiBH_4(s) + CeH_2(s) \quad \longrightarrow \quad 6LiH(s) + CeB_6(s) + 10H_2(g) \quad (7.4 \text{ wt. \%}) \quad (2.5)$$

$$6LiBH_4(s) + CaH_2(s) \quad \longrightarrow \quad 6LiH(s) + CaB_6(s) + 10H_2(g) \quad (11.7 \text{ wt. \%}) \quad (2.6)$$
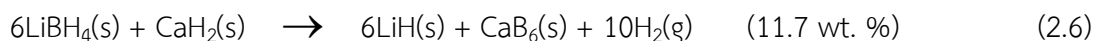
Moreover, the composites of $LiBH_4$-$NaAlH_4$ with and without $TiCl_3$ were studied (Shi, Yu, Feidenhans, and Vegge, 2008). Firstly, the formations of $NaBH_4$ and $LiAlH_4$ were observed after ball milling due to the reaction between $LiBH_4$ and $NaAlH_4$ (equation (2.7)). Due to catalytic effect of $TiCl_3$, $LiAlH_4$ decomposed to Li_3AlH_6, Al, and H_2 at room temperature (equation (2.8)) and Li_3AlH_6 further desorbed hydrogen at 100 °C (equation (2.9)) (ΔT= 135 and 110 °C, with respect to bulk $LiAlH_4$ and Li_3AlH_6, respectively). Moreover, the formation of $LiNa_2AlH_6$ was found in the $LiBH_4$-$NaAlH_4$ composites with $NaAlH_4$ rich (e.g., $2LiBH_4$-$3NaAlH_4$). This limited rehydrogenation reaction and led to the reduction of hydrogen capacity in further cycles. Although dehydrogenation kinetics of $LiAlH_4$ improved significantly, $NaBH_4$ decomposing at high temperature (above 400 °C) still obstructed practical use of this material.
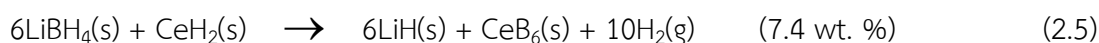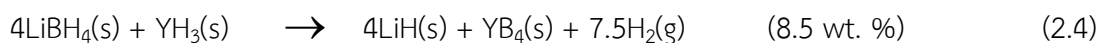
$$LiBH_4(s) + NaAlH_4(s) \quad \longrightarrow \quad LiAlH_4(s) + NaBH_4(s) \quad (2.7)$$

$$3LiAlH_4(s) \quad \longrightarrow \quad Li_3AlH_6(s) + 2Al(s) + 3H_2(g) \quad (2.8)$$

$$Li_3AlH_6(s) \quad \longrightarrow \quad 3LiH(s) + Al(s) + 3/2H_2(g) \quad (2.9)$$
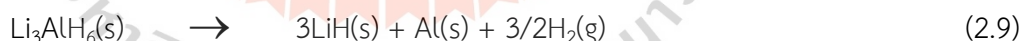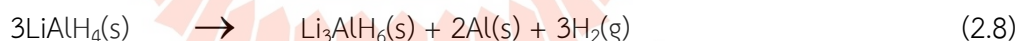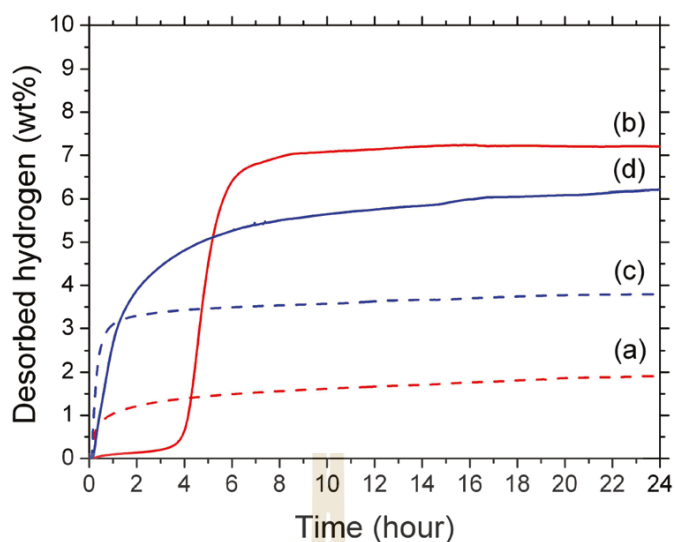
Figure 2.5 Dehydrogenation profiles at 350 °C of $4LiBH_4 + YH_3$ composites under (a) vacuum and (b) 3 bar H_2, and $6LiBH_4 + CeH_2$ composite under (c) vacuum (d) 3 bar H_2 (Shim et al., 2009).

Furthermore, Liu et al. (2016) studied the dehydrogenation properties of $2LiBH_4 + Al$ and $2LiBH_4 + AlH_3$. Superior dehydrogenation kinetics of $2LiBH_4 + AlH_3$ to $2LiBH_4 + Al$ and bulk $LiBH_4$ was found (Figure 2.6). $2LiBH_4 + AlH_3$ released hydrogen in two steps with 9 wt. % H_2 within 1 h. The formations of AlB_2 and Li-Al-B during dehydrogenation contributed to the improvement of hydrogen desorption properties of $LiBH_4$. However, agglomeration of sample after dehydrogenation was observed, leading to the inferior performance in the next cycles.
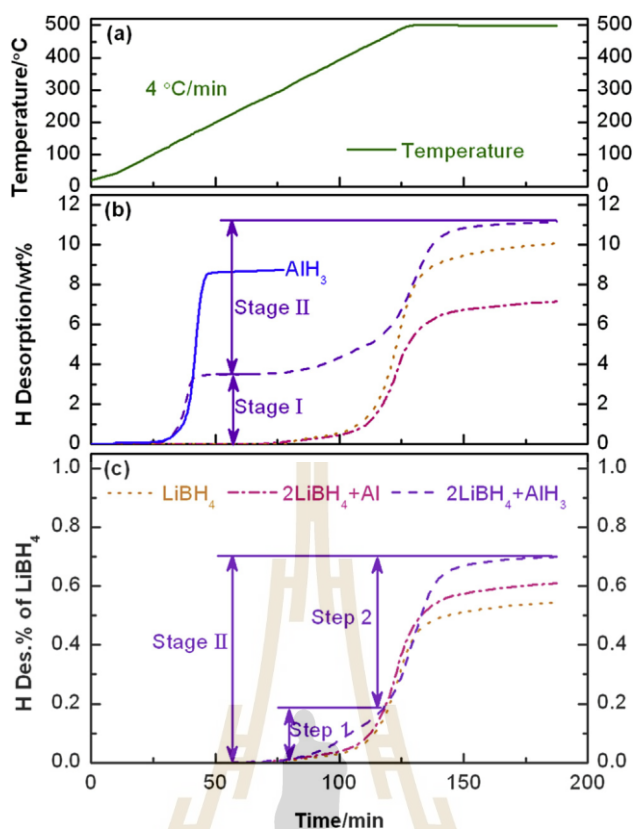
Figure 2.6 Hydrogen desorption behaviors of as-prepared AlH_3, as-milled $2LiBH_4 + AlH_3$, $2LiBH_4 + Al$, and $LiBH_4$ during heating process: (a) temperature program, (b) hydrogen desorption capacity (wt. %), (c) fractional hydrogen desorption of $LiBH_4$ in samples (Liu et al., 2016).

Other composites of $LiBH_4$-$LiAlH_4$ and $LiBH_4$-Li_3AlH_6 with and without transition metal-based catalysts (e.g., TiF_3, $TiCl_3$, and Ti-isopropoxide) (Mao, Guo, Liu, and Yu, 2009; Wu et al., 2012; Natthaporn Thaweelap and Rapee Utke, 2016; Meggouh, Grant, Walker, 2011; Soru et al., 2014) proceeded comparable reaction mechanisms of (i) dehydrogenation of $LiAlH_4$ and Li_3AlH_6, (ii) reaction between $LiBH_4$ and Al, (iii) individual dehydrogenation of $LiBH_4$, and (iv) reaction between LiH and Al. Upon dehydrogenation, the formations of several phases, such as Al, LiH, amorphous B, and $Li_2B_{12}H_{12}$ have been observed together with active species of AlB_2, Li-Al-B, and LiAl, benefiting hydrogen sorption kinetics and reversibility. Kinetics and thermodynamics of $LiBH_4$ were improved by compositing with $LiAlH_4$ and Li_3AlH_6 (Mao et al., 2009; Wu et al., 2012; Natthaporn Thaweelap and Rapee Utke, 2016; Meggouh et al., 2011) for example, 5 mol% TiF_4-doped $LiBH_4$-$LiAlH_4$ showed the reduction of dehydrogenation enthalpy and onset temperature by 14 kJ/mol H_2 and 150 °C, respectively, with respect to pristine $LiBH_4$ (Mao et al., 2009). The $LiBH_4$-Li_3AlH_6 composites released total capacity of 8.5 wt. % H_2 at T< 450 °C as well as the decrease of onset dehydrogenation temperatures of Li_3AlH_6 and $LiBH_4$ by 20 and 50 °C, respectively (Wu et al., 2012).
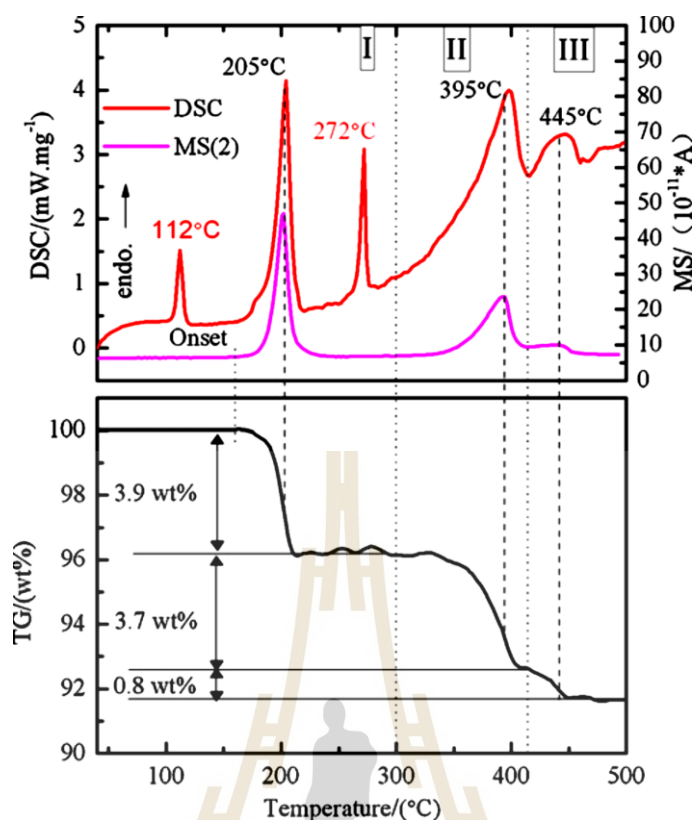
Figure 2.7 TG/DSC/MS profiles of LiBH$_4$/Li$_3$AlH$_6$ composites at a heating rate of 5 °C min^{-1} (Wu et al., 2012).

Figure 2.7 shows the TG/DSC/MS profiles of LiBH$_4$/Li$_3$AlH$_6$ composites. There are five endothermic peaks of DSC during the dehydrogenation of the LiBH$_4$/Li$_3$AlH$_6$ composites at 112, 205, 272, 395, and 445 °C. The endothermic peaks at 112 and 272 °C correspond to the phase transformation and melting temperatures of LiBH$_4$, respectively. In the MS signal, three peaks of desorbed hydrogen are observed. These related to weight losses at 205, 395, and 445 °C, respectively (TG signal). This can be concluded that three endothermic reactions at 205, 395, and 445 °C correspond to hydrogen release in the three-step dehydrogenation of the LiBH$_4$/Li$_3$AlH$_6$ composites.

However, the formation of AlB$_2$ layer around Al particles during dehydrogenation, yielding to deficient free surface of Al to react with LiBH$_4$ or LiH to further produce AlB$_2$ and other active species (Li-Al-B, and LiAl) resulted in poor reversibility of LiBH$_4$ (Meggouh et al., 2011). Although LiAlH$_4$ showed good dispersion in LiBH$_4$ after ball milling due to its brittleness, this advantage was lost when it melted upon heating, leading to agglomeration of metallic Al (Figure 2.8) (Meggouh et al., 2011). Moreover, considerable amount of metallic Al formed after dehydrogenation of LiBH$_4$-LiAlH$_4$ (or LiBH$_4$-Li$_3$AlH$_6$) with and without catalysts resulted in irreversibility of LiAlH$_4$ and/or Li$_3$AlH$_6$ despite high temperature and

pressure applied for rehydrogenation (T= 400-600 °C and p(H$_2$)= 40-80 bar) (Mao et al., 2009; Wu et al., 2012; Natthaporn Thaweelap, and Rapee Utke, 2016).
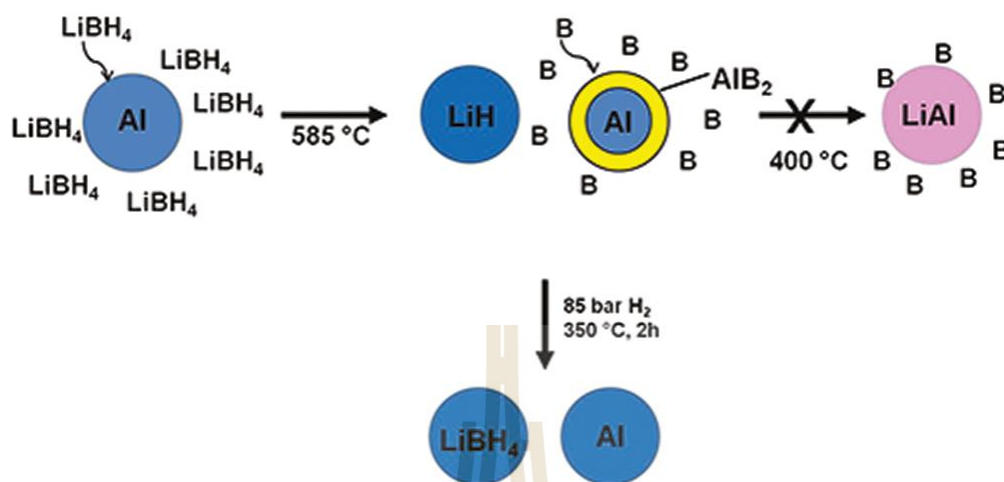
Figure 2.8 Schematic representation of the formation of an AlB$_2$ shell around an Al particle preventing the formation of LiAl and the reformation of LiBH$_4$ (Meggouh et al., 2011).

From Figure 2.8, the product of reaction between LiBH$_4$ and Al are LiH, amorphous B, Al, and AlB$_2$. However, the formation of LiAl is not observed. This could be explained that Al particles are covered by amorphous B and AlB$_2$. These barriers prevent unreacted Al to form LiAl and fully AlB$_2$ conversion. Therefore, LiBH$_4$ revealed poor recovered after rehydrogenation and capacity in the 2nd cycle decreased.

In the present work, we would like to propose the simple strategy to enhance surface area and particle distribution of all phases, especially Al by ball milling the dehydrogenated sample of LiBH$_4$-LiAlH$_4$ composites quenched at the first-step reaction (decomposition of LiAlH$_4$ at 220 °C). In addition, multi-walled carbon nanotubes (MWCNTs), benefiting hydrogen diffusion and thermal conductivity during de/rehydrogenation as well as preventing particle agglomeration and/or sintering upon cycling (Ruffieux, Gröning, O., Bielmann, and Gröning, P., 2004; Sophida Thiangviriya and Rapee Utke, 2016; Adelhelm, and Jongh, 2011; Chaise et al., 2009; Praphatsorn Plerdsranoy, Songwuti Chanthee, and Rapee Utke, 2017) are doped into the milled sample.

2.3   References

Adelhelm, P., and de Jongh, P. E. (2011). The impact of carbon materials on the hydrogen storage properties of light metal hydrides. *J. Mater Chem., 21,* 2417-2427.

Au, M., Jurgensen, A., and Zeigler, K. (2006). Modified lithium borohydrides for reversible hydrogen storage (2). *J. Phys. Chem. B., 110,* 26482-26487.

Au, M., Spencer, W., Jurgensen, A., and Zeigler, C. (2008). Hydrogen storage properties of modified lithium borohydrides. *J. Alloys Compd., 462,* 303-309.

Bösenberg, U., Doppiu, S., and Mosegaard, L. (2007). Hydrogen sorption properties of MgH_2-$LiBH_4$ composites. *Acta. Mater., 55,* 3951-3958.

Bogdanovic, B., and Schwickardi, M. (1997). Ti-doped alkali metal aluminium hydrides as potential novel reversible hydrogen storage materials. *J. Alloys Compd., 253- 254,* 1-9.

Chaise, A., de Rango, P., Marty, Ph., Fruchart, D., Miraglia, S., Olivès, R., and Garrier, S. (2009). Enhancement of hydrogen sorption in magnesium hydride using expanded natural graphite. *Int. J. Hydrogen Energy., 34,* 8589-8596.

Fang, Z. Z., Kang, X. D., and Wang, P. (2010). Improved hydrogen storage properties of $LiBH_4$ by mechanical milling with various carbon additives. *Int. J. Hydrogen Energy., 35,* 8247-8252.

Fu, Q. J., Ramirez-Cuesta, A. J., and Tsang, S. C. (2006). Molecular aluminum hydrides identified by inelastic neutron scattering during H_2 regeneration of catalyst-doped $NaAlH_4$. *J. Phys. Chem. B., 11,* 711-715.

Gross, A. F., Vajo, J. J., Van Atta, S. L., and Olson, G. L. (2008). Enhance hydrogen storage kinetics in nanoporous carbon scaffold. *J. Phys. Chem. C., 112,* 5651-5657.

Guo, Y., Wu, H., Zhou, W., and Yu, X. (2011). Dehydrogenation tuning of ammine borohydrides using double-metal cations. *J. Am. Chem, Soc, 133,* 4690-4693.

Guo, Y. H., Yu, X. B., Gao, L., Xia, G. L., Guo, Z. P., and Liu H. K. (2009). Significantly improved dehydrogenation of $LiBH_4$ destabilized by TiF_3. *Energy Environ. Sci., 3,* 465-470.

Kang, X. D., Wang, P., Ma, L. P., and Cheng, H. M. (2007). Reversible hydrogen storage in $LiBH_4$ destabilized by milling with Al. *Appl. Phys. A., 89,* 963-966.

Kou, H., Sang, G., Zhou, Y., Wang, X., Huang, Z., Luo, W., Chen, L., Xiao, X., Yang, G., and Hu, C. (2014). Enhanced hydrogen storage properties of $LiBH_4$ modified by NbF_5. *Int. J. Hydrogen Energy., 39,* 11675-11682.

Li, C., Peng, P., Zhou, D. W., and Wan, L. (2011). Research progress in $LiBH_4$ for hydrogen storage: A review. *Int. J. Hydrogen Energy., 36,* 14512-14526.

Liu, H., Wang, X., Zhou, H., Gao, S., Ge, H., Li, S., and Yan, M. (2016). Improved hydrogen desorption properties of $LiBH_4$ by AlH_3 addition. *Int. J. Hydrogen Energy., 41,* 22118-22127.

Mao, J. F., Guo, Z. P., Liu, H. K., and Yu, X. B. (2009). Reversible hydrogen storage in titanium-catalyzed LiAlH$_4$-LiBH$_4$ system. *J. Alloy Compd., 487,* 434-438.

Mauron, P., Buchter, F., and Friedrichs, O. (2008). Stability and reversibility of LiBH$_4$. *J. Phys. Chem. B., 112,* 906-910.

Meggouh, M., D. M. Grant, D. M., and Walker, G. S. (2011). Optimizing the Destabilization of LiBH$_4$ for Hydrogen Storage and the Effect of Different Al Sources. *J. Phys. Chem. C., 115,* 22054-22061.

Orimoa, S., Nakamoria, Y., and Kitaharaa, G. (2005). Dehydriding and rehydriding reactions of LiBH$_4$. *J. Alloys Compd., 404-406,* 427-430.

Plerdsranoy, P., Chanthee, S., and Utke, R. (2017). Compaction of LiBH$_4$-MgH$_2$ doped with MWCNTs-TiO$_2$ for reversible hydrogen storage. *Int. J. Hydrogen Energy., 42,* 978-986.

Ravnsbæk, D. B., and Jensen, T. R. (2012). Mechanism for reversible hydrogen storage in LiBH$_4$-Al. *J. Appl. Phys., 111,* 112621.

Rongeata, C., Annac, V. D., Hagemannc, H., Borgschulteb, A., Züttelb, A., Schultza, L., and Gutfleischa, O. (2010). Effect of additives on the synthesis and reversibility of Ca(BH$_4$)$_2$. *J. Alloys Compd., 493,* 281-287.

Ruffieux, P., Gröning, O., Bielmann, M., and Gröning, P. (2004). Hydrogen chemisorption on sp^2-bonded carbon: Influence of the local curvature and local electronic effects. *Appl. Phys. A., 78,* 975-980.

Shi, Q., Yu, X., Feidenhans, I. R., and Vegge, T. (2008). Destabilized LiBH$_4$-NaAlH$_4$ mixture doped with titanium based catalysts. *J. Phys. Chem. C., 112,* 18244-18248.

Shim, J. H., Lim, J. H., Rather, H., Lee, Y. S., Reed, D., Kim, Y., Book, D., and Cho, Y. W. (2009). Effect of hydrogen back pressure on dehydrogenation behavior of LiBH$_4$-based reactive hydride composites. *J. Phys. Chem. Lett., 1,* 59-63.

Silvearv, F. (2011). First principle studies of functional materials. *Hydrogen storage and cutting tools.* (pp. 37-44). Sweden: Acta Universitatis Upsaliensis.

Soru, S., Taras, A., Pistidda, C., Milanese, C., Bonatto Minella, C., Masolo, E., Garroni, S. (2014). Structural evolution upon decomposition of the LiAlH$_4$+LiBH$_4$ system. *J. Alloys Compd., 615,* S693-S697.

Sun, D., Srinivasan, S. S., Kiyobayashi, T., Kuriyama, N., and Jensen, C. M. (2003). Rehydrogenation of dehydrogenated NaAlH$_4$ at low temperature and pressure. *J. Phys. Chem. B., 17,* 1176-10179.

Sutton, A. D., Burrell, A. K., Dixon, D. A., Garner, E. B., Gordon, J. C., Nakagawa T., Ott, K. C., Robinson, J. P., and Vasiliu, M. (2011). Regeneration of ammonia borane spent fuel by direct reaction with hydrazine and liquid ammonia. *Science., 331,* 1426-1429.

Thaweelap, N., and Utke, R. (2016). Dehydrogenation kinetics and reversibility of LiAlH$_4$-LiBH$_4$ doped with Ti-based additives and MWCNT. *J. Phys. Chem. Solids., 98,* 149-155.

Thiangviriya, S., and Utke, R. (2016). Improvement of dehydrogenation kinetics of 2LiBH$_4$-MgH$_2$ composite by doping with activated carbon nanofibers. *Int. J. Hydrogen Energy., 41,* 2797-2806.

Vajo, J. J., and Olson, G. L. (2007*).* Hydrogen storage in destabilized chemical systems. *Scr. Mater., 56,* 829-834.

Vajo, J. J., Salguero, T. T., and Gross, A. F. (2007). Thermodynamic destabilization and reaction kinetics in light metal hydride systems. *J. Alloys Compd., 446-447,* 409-414.

Vajo, J. J., and Skeith, S. L. (2005). Reversible storage of hydrogen in destabilized LiBH$_4$. *J. Phys. Chem. B., 109,* 3719-3722.

Wang, K., Kang, X., Ren, J., and Wang, P. (2016). Nanostructured graphite-induced destabilization of LiBH$_4$ for reversible hydrogen storage. *J. Alloys Compd., 685,* 242-247.

Wu, X., Wang, X., Cao, G., Li, S., Ge, H., Chen, L., and Yan, M. (2012). Hydrogen storage properties of LiBH$_4$-Li$_3$AlH$_6$ composites. *J. Alloy Compd., 517,* 127-131.

Weiqing, J., and Shilong, C. (2017). Effect of Al on the dehydrogenation of LiBH$_4$ from first-principles calculations. *Int. J. Hydrogen Energy., 42,* 6181-6188.

Xiong, Z., Yong, C. K., Wu, G., Chen, P., Shaw, W., Karkamkar, A., and David, W. I. F. (2007). High-capacity hydrogen storage in lithium and sodium amidoboranes. *Nat. Mater., 7,* 138-141.

Zhang, Y. H., Ding, H., Liu, C., Zhang, S. L., and Huang, S. P. (2013). Significant effects of graphite fragments on hydrogen storage performances of LiBH$_4$: a first principles approach. *Int. J. Hydrogen Energy., 38,* 13717-13727.

Zhu, Y., Zou, J., and Zeng, X. (2015). Study on reversible hydrogen sorption behaviors of 3LiBH$_4$/graphene and 3LiBH$_4$/graphene–10 wt% CeF$_3$ composites. *RSC. Adv., 5,* 82916-82923.

Züttel, A., Remhof, A., Borgschulte, A., and Friedrichs, O. (2010). Hydrogen: the future energy carrier. *Phil. Trans. R. Soc. A., 368,* 3329-3342.

Züttel, A., Wenger P., and Rentsch, S. (2003). LiBH$_4$ a new hydrogen storage material. *J. Power Sources., 118,* 1-7.

CHAPTER III

EXPERIMENTS

3.1   Sample Preparations

The LiBH$_4$ (≥90% hydrogen-storage grade, Sigma-Aldrich) and LiAlH$_4$ (>99.95% hydrogen-storage grade, Sigma-Aldrich) were milled with a molar ratio of 1:1 in a stainless-steel vial (Evico Magnetic, Germany) using a SPEX SamplePrep 8000D DUAL Mixer/Mill (Figure 3.1B) to obtain LiBH$_4$-LiAlH$_4$ composite, denoted as LB-LA. Milling time and ball-to-powder weight ratio (BPR) were 5 h and 10:1, respectively. The LB-LA was dehydrogenated at 220 °C for 15 min and milled for 5 h with BPR of 10:1, and denoted as LB-LA (220). The MWCNTs (Nano Generation Co. Ltd., Thailand) were treated at 100 °C under vacuum for 1 h to remove oxygen and moisture. Treated MWCNTs (5 wt %) were milled with LB-LA (220) for 30 min with BPR of 10:1 to obtain LB-LA (220) doped with 5 wt % MWCNTs, denoted as LB-LA (220)-CNT. All samples were handled under a nitrogen atmosphere in a glove box (99.9% N$_2$) (Omni-Lab System, VAC) (Figure 3.1A).
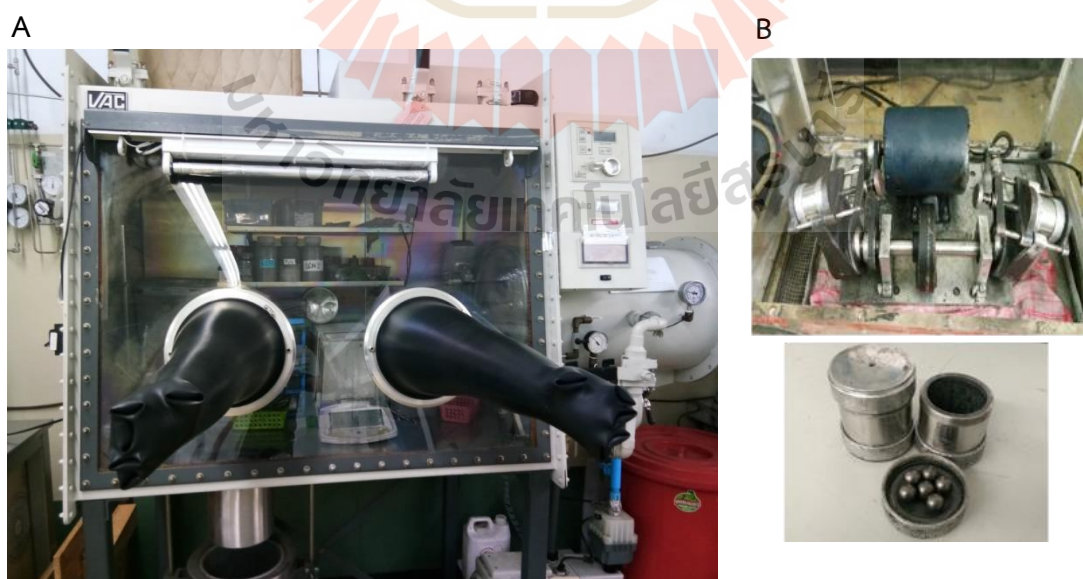

Figure 3.1 Glove box (Omni-Lab System, VAC) (A) and SPEX SamplePrep 8000D DUAL Mixer/Mill and stainless-steel vial (B)**.**

3.2   Characterizations

3.2.1 Powder X–ray diffraction (XRD)

Powder X–ray diffraction (XRD) of as-prepared and de/rehydrogenated powder samples were carried out by using a Bruker D2 PHASER with Cu K$_\alpha$ radiation (λ = 1.5406 A°) (Figure 3.2A). The sample of approximately 7-10 g was packed in an airtight sample holder, covered by a poly (methyl methacrylate) dome (Figure 3.2B). All XRD experiments were conducted at room temperature. The scanning step was 0.02 °/s. The scanning 2θ was in the range of 10-80°.

A   B
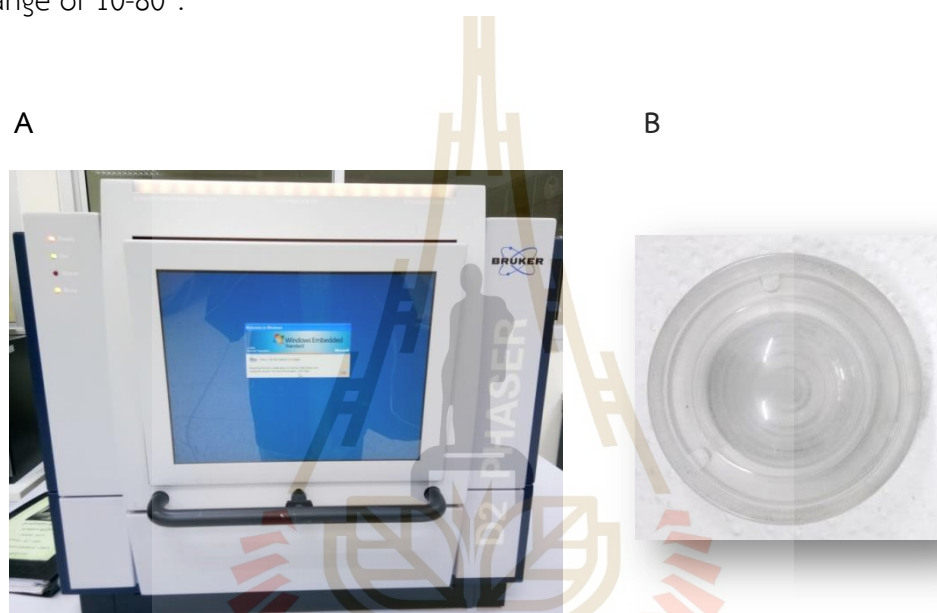
Figure 3.2 A Bruker D2 Phaser Powder X–ray diffractometer (A) and sample holder, covered by a poly (methyl methacrylate) dome (B).

3.2.2 Fourier transform infrared spectroscopy (FTIR)

The powder samples of milled LB-LA, LB-LA (220), and LB-LA (220)-CNT were investigated by Fourier Transform Infrared Spectrophotometer (FTIR) using a Bruker Tensor 27-Hyperion 2000 (Figure 3.3). The mixture of sample powder and anhydrous KBr was ground in the mortar with the weight ratio of ~1:10 (sample powder: KBr), and pressed under a specific pressure into a pellet of 1 cm diameter. The KBr pellet containing the sample was assembled in the instrument, where it was on the infrared direction. The spectra were collected in the wavenumber range of 4000-400 cm^{-1} with 64 scans for both sample and background. To accomplish the final spectrum, subtraction of the sample spectrum with that of the background was done.

Figure 3.3 A Bruker Tensor 27 Fourier transform infrared spectrophotometer.

3.2.3 X-ray photoelectron spectroscopy (XPS)

The X-ray photoelectron spectroscopy (XPS) was carried out at the SUT-NANOTEC-SLRI joint research facility, Synchrotron Light Research Institute (Public Organization), Thailand (Figure 3.4), using a PHI5000 Versa Probe II (ULVAC-PHI Inc., Japan) with Al K$_\alpha$ (1.486 keV) radiation as an excitation source. The powder samples were deposited on the sample holders by using carbon glue tape in the glove box under N_2 atmosphere. Prior to the measurements, all prepared samples were placed in a high vacuum chamber (1×10^{-8} mbar) for 2 h. The high-resolution scan of each element was collected using pass energy and a step size of 46.95 and 0.05 eV, respectively. Dual-beam charge neutralization (low energy electron and ion beam) method was used to minimize sample charging. The binding energy was calibrated with respect to the C 1s peak (284.8 eV). The data were processed and analyzed using MultiPak software version 9.6.0 (ULVAC-PHI, Japan). Peak fitting was performed after Shirley background subtraction and a symmetrical Gaussian–Lorentzian function was used to approximate the line shapes of the fitting components.
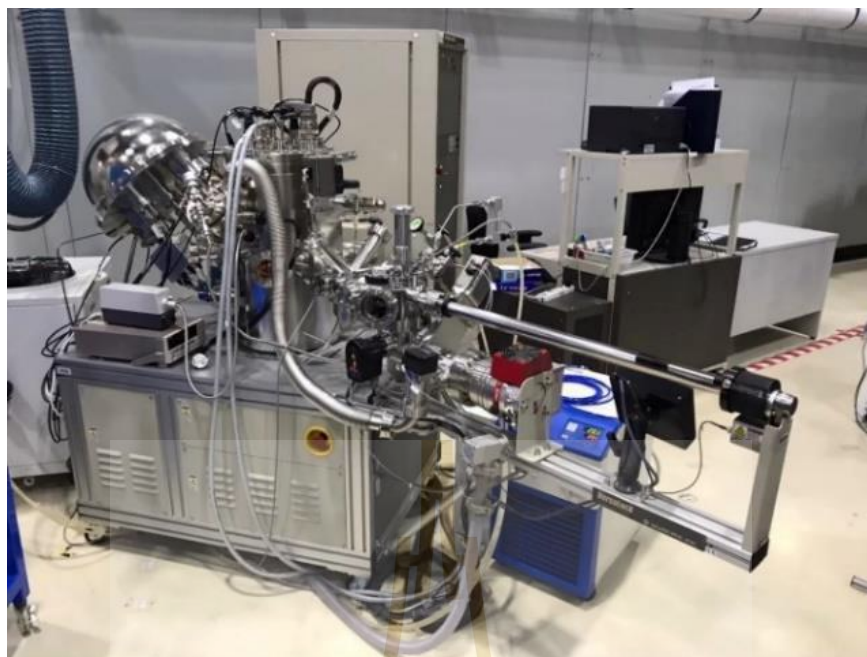
Figure 3.4 X-ray photoelectron spectroscopy at Synchrotron Light Research Institute (SLRI).

3.2.4 Solid-state nuclear magnetic resonance spectroscopy (NMR)

Solid-State ^{27}Al, magic-angle spinning nuclear magnetic resonance (MAS NMR) spectra were recorded by a Bruker ASCEND^{TM} 500 spectrometer (Figure 3.5A). The samples were tightly packed in a zirconia end-capped tube (Figure 3.5B). All experiments were performed at 302 K using a BL4 VTN probe for 4 mm outer diameter rotors. The ^{27}Al chemical shifts were detected in parts per million (ppm) relative to neat aluminum oxide (Al_2O_3). Spinning speed (υ_R), excitation pulse length, and the number of scans were 8 kHz, 9.8 μs, and 1000, respectively.

A   B

Figure 3.5 A Bruker Ascend™ 500 Solid-State magic-angle spinning nuclear magnetic resonance (MAS NMR) spectrometer (A) and zirconia end-capped tube (B).

3.2.5 Optical microscopy

Morphology of samples was characterized using an optical microscope (BX51, Olympus America Inc., USA) (Figure 3.6A). As-prepared LB-LA, LB-LA (220), and LB-LA (220)-CNT were sandwiched between microscope glass slides wrapped with Kapton tape to prevent oxidation from air and moisture (Figure 3.6B). The experiments were carried out under LBD, ND25, and ND6 transmitted light and all micrographs were collected using an Olympus XC50 camera with a color charge-coupled device.
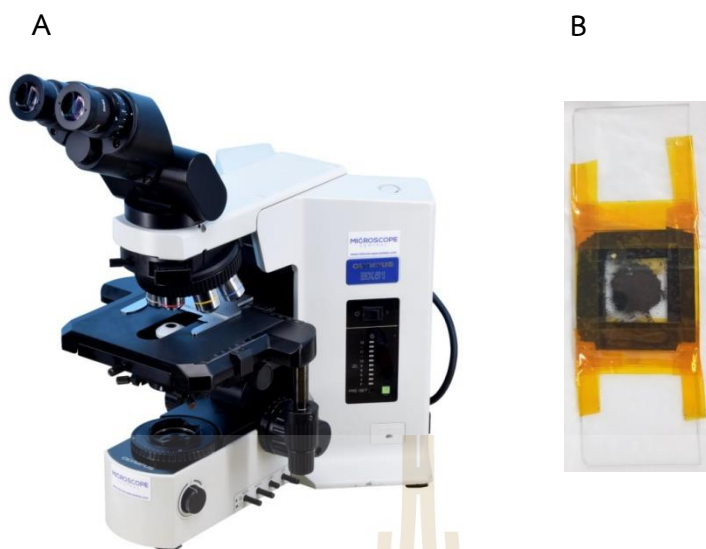
A   B

Figure 3.6 An Olympus optical microscopes (A) and sandwiched glass slides of sample. (B) (https://microscopecentral.com/products/olympus-bx51-microscope).

3.2.6   Kinetic measurements

Dehydrogenation kinetics and reversibility were investigated using a laboratory-scale setup of a Sievert–type apparatus (Figure 3.7 and 3.8) (Rapee Gosalawit-Utke et al., 2014). The powder samples (100-200 mg) was packed in a high pressure stainless steel sample holder (316SS, Swagelok) under argon atmosphere of the glove box and transferred to the Sievert-type apparatus. Two K-type thermocouples (-250–1,300 °C, SL heater) were attached to the sample holder and the furnace to measure the temperature of the system. Pressure transducers (C206, Cole Parmer) in the pressure range of 0-500 psig and 0-3000 psig were used to measure the pressure change due to hydrogen desorption and absorption, respectively. Thermocouples and pressure transducers were connected to an AI 210I module convertor data logger (Wisco), measuring and transferring (every 1 s) the pressure and temperature changes of the sample to the computer for further evaluation. Dehydrogenation was carried out at 400 °C under 7 mbar H_2 and rehydrogenation was at 400 °C under 80 bar H_2 for 16 h. Once the pressure of the system was constant, the amount of hydrogen released was calculated by the pressure change (Δp) and the following equations: Once the pressure reading was constant over a period of time, the amount of hydrogen release and uptake was calculated by the pressure change (ΔP) using the following equations:

$$(\Delta P)V = nRT \tag{3.1}$$

$$H_2 \text{ desorbed (wt. \%)} = [(n \times 2.0158)/\text{sample weight}] \times 100 \tag{3.2}$$

where P, V, and T are hydrogen pressure (atm), volume of the system (L), and temperature (K), respectively, n is the number of hydrogen moles (mol), and R is gas constant (0.0821 L atm K^{-1} mol^{-1}).

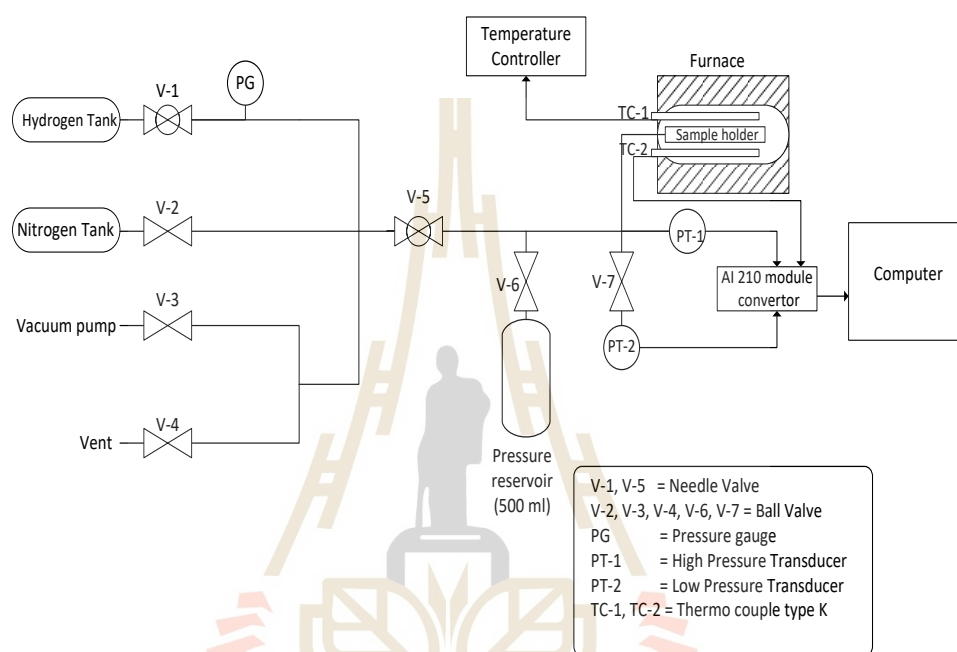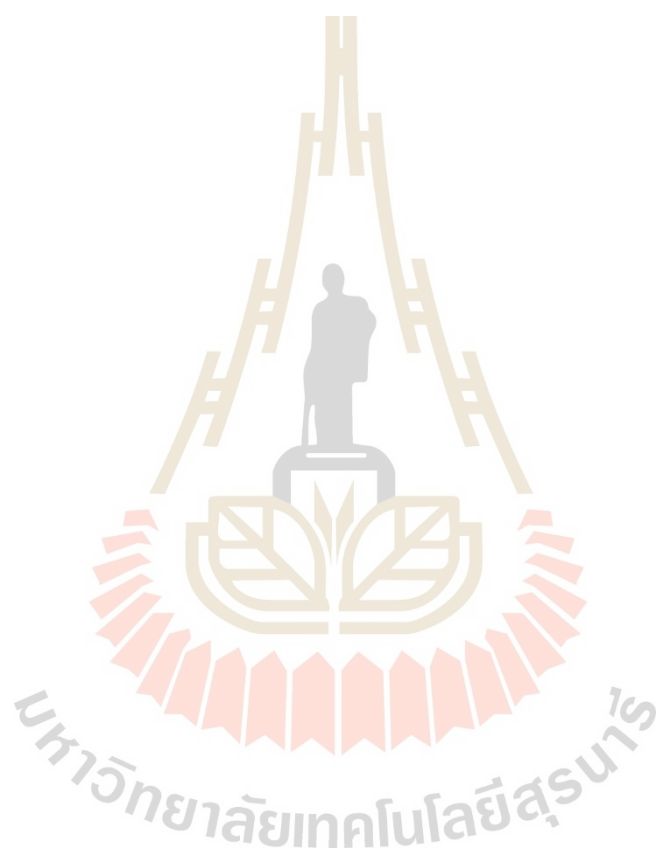**Figure 3.7** Schematic diagram of Sievert–type apparatus.

Figure 3.8 Laboratory-scale setup of Sievert–type apparatus.

3.3 References

Gosalawit-Utke, R. Meethom, S. Pistidda, C., Milanese, C., Laipple, D., Saisopa, T., and Dornheim, M. (2014). Destabilization of $LiBH_4$ by nanoconfinement in PMMA-co-BM polymer matrix for reversible hydrogen storage. *Int. J. Hydrogen Energy., 39,* 5019–5029.

CHAPTER IV
RESULTS AND DISCUSSION

4.1   Results and Discussion

4.1.1 Investigation of phase compositions

Phase compositions of as-prepared LB-LA, LB-LA (220), and LB-LA (220)-CNT are investigated by PXD, FTIR, and B 1s XPS techniques. The diffraction pattern of LB-LA shows the signals of $LiAlH_4$, $LiBH_4$, Li_3AlH_6, and Al/LiH (Figure 4.1(a)), while those of LB-LA (220) and LB-LA (220)-CNT reveal comparable phases of $LiBH_4$ and Al/LiH (Figure 4.1(b) and (c)). Due to small and broad diffraction peaks of $LiBH_4$ observed in PXD patterns, especially those of LB-LA (220) and LB-LA (220)-CNT (Figure 4.1(b) and (c)), FTIR and B 1s XPS experiments are further carried out to track B-containing phases.
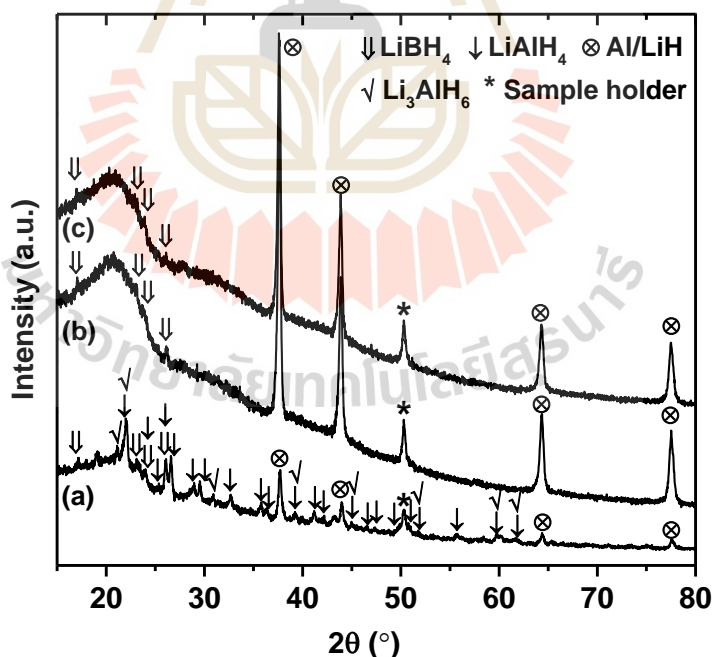

Figure 4.1 PXD spectra of as-prepared LB-LA (a), LB-LA (220) (b), and LB-LA (220)-CNT (c).

FTIR spectra of all as-prepared samples show vibrational peaks of B–H stretching and bending of LiBH$_4$ (2387-2227 and 1122 cm^{-1}, respectively) (Zhao et al., 2017), O–H bending of air and/or moisture contamination during experiments (1636 cm^{-1}) (Rapee Gosalawit-Utke et al., 2014), and B–O asymmetric stretching due to oxidation of LiBH$_4$ (1600-1300 cm^{-1}) (B€osenberg, 2010; Kamitsos, Karakassides, and Chryssikos, 1987) (Figure 4.2).
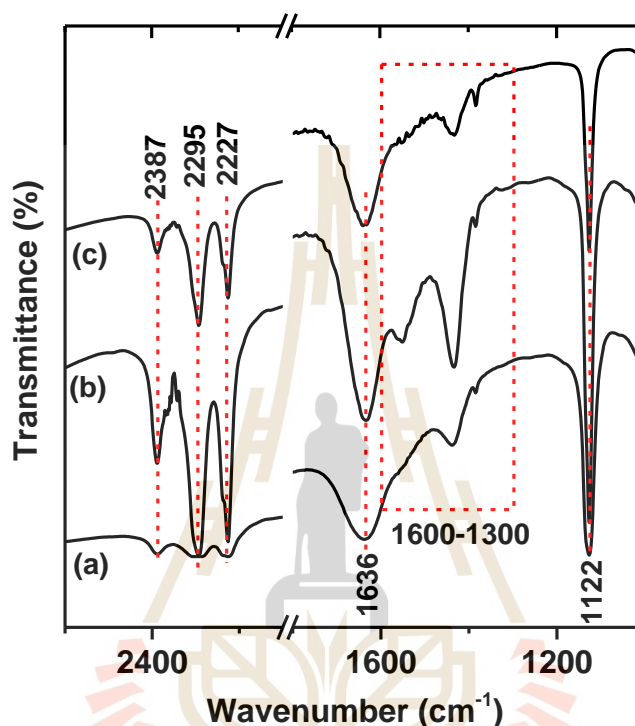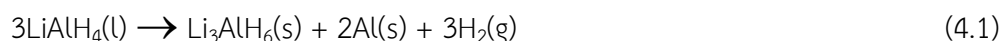

Figure 4.2 FTIR spectra of as-prepared LB-LA (a), LB-LA (220) (b), and LB-LA (220)-CNT (c).

Moreover, B 1s XPS spectra of all as-prepared samples show characteristic peaks of B–H bond of LiBH$_4$ (187.8-188.3 eV) and B–O bond of B$_2$O$_3$ due to oxidation of LiBH$_4$ (192 eV) (Figure 4.3) (Sophida Thiangviriya and Rapee Utke, 2016; U.S. Department of Commerce, 2012; Deprez et al., 2011). The signal of B–O bond implies oxidation with air and/or moisture of B-containing phases, i.e. LiBH$_4$ and/or amorphous B obtained from decomposition of LiBH$_4$ during ball milling. Thus, the weak LiBH$_4$ diffraction peaks in LB-LA (220) and LB-LA (220)-CNT (Figure 4.1(b) and (c)) can be explained by nanocrystallite size and/or amorphous state due to ball milling. The formation of Li$_3$AlH$_6$ and Al/LiH detected in LB-LA suggests partial dehydrogenation of LiAlH$_4$ (equation (4.1)) during ball milling. In the case of as-prepared LB-LA (220) and LB-LA (220)-CNT, the signal of Al/LiH hints at complete dehydrogenation of LiAlH$_4$ to LiH and Al at 220 °C (equation (4.1) and (4.2)).

$$3LiAlH_4(l) \longrightarrow Li_3AlH_6(s) + 2Al(s) + 3H_2(g) \tag{4.1}$$

$$Li_3AlH_6(s) \longrightarrow 3LiH(s) + Al(s) + 3/2H_2(g) \qquad (4.2)$$
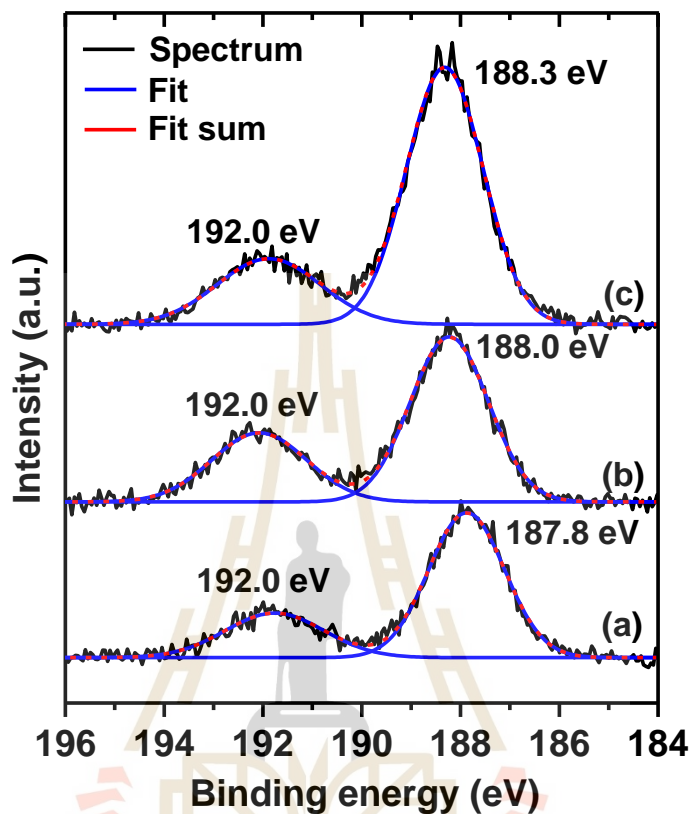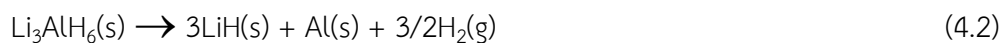
Figure 4.3 B 1s XPS spectra of as-prepared LB-LA (a), LB-LA (220) (b), and LB-LA (220)-CNT (c).

4.1.2 Morphological studied

The morphology of all as-prepared samples is characterized by optical microscopy. The LB-LA (220) and LB-LA (220)-CNT (Figure 4.4B and C) show smaller particles and less agglomeration as compared with LB-LA (Figure 4.4A). This confirms that particle size reduction can be obtained after ball milling of dehydrogenated LB-LA quenched at 220 °C, leading to high reactive surface area and good dispersion of all phases.

Figure 4.4 Micrographs of LB-LA (A), LB-LA (220) (B), and LB-LA (220)-CNT (C).

4.1.3 The first dehydrogenation kinetics

The 1st dehydrogenation kinetics (T= 400 °C and p(H$_2$)= 7 mbar H$_2$) of all as-prepared samples is investigated. The LB-LA releases hydrogen in two steps with total storage capacity of 6.2 wt. % H$_2$ (Figure 4.5), approaching the results from the previous studies (6.10 wt. % H$_2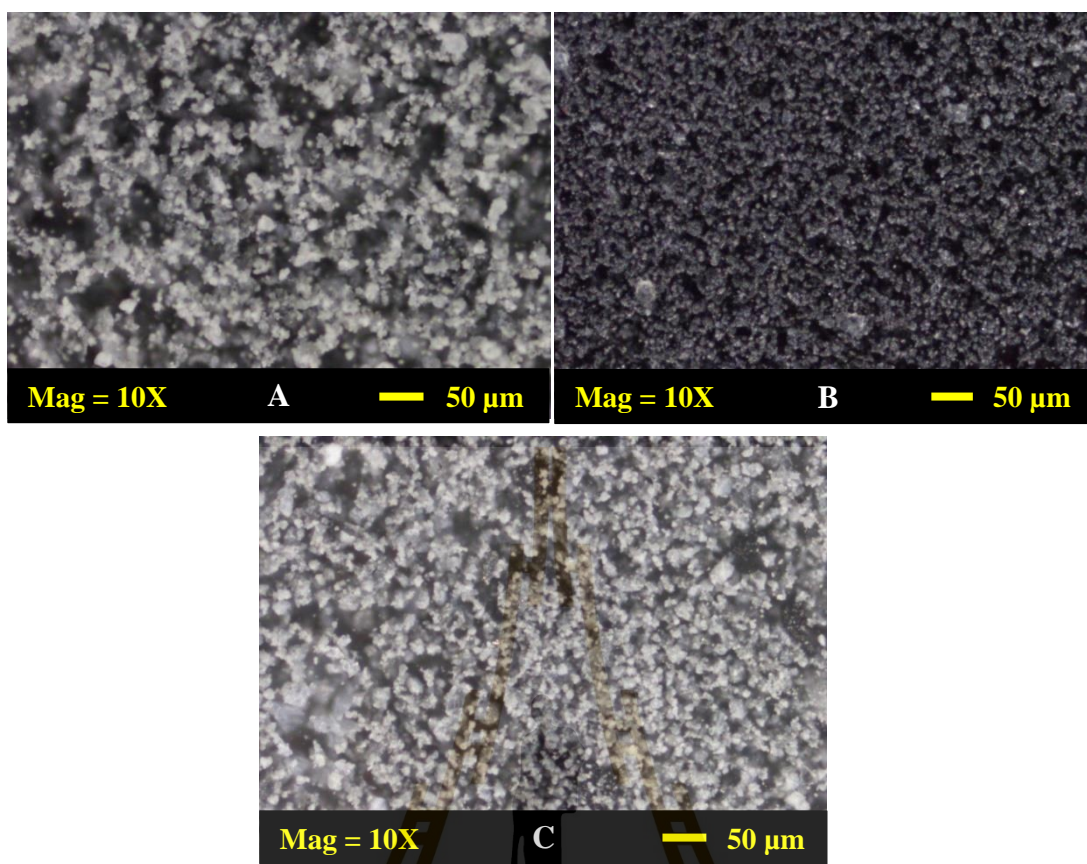$) (Praphatsorn Plerdsranoy and Rapee Utke, 2015). The first-step reaction (T= 100-250 °C) rapidly liberating ~4.0 wt. % H$_2$ within 2 h agrees with decompositions of LiAlH$_4$ and Li$_3$AlH$_6$ (equations (4.1) and (4.2)). For the 2nd step corresponding to decomposition of LiBH$_4$, onset temperature at 364 °C is observed with storage capacity of 2.2 wt. % H$_2$ within 6 h. For LB-LA (220) and LB-LA (220)-CNT, single-step dehydrogenation is detected (Figure 4.5). The 1st step reaction is not observed due to complete dehydrogenation of LiAlH$_4$ during sample preparation, in accordance with PXD results (Figure 4.1(b) and (c)). During the 2nd step, decomposition of LiBH$_4$ releases 2.7-3.0 wt. % H$_2$ within 2 h (~three times faster kinetics) at significant lower onset temperature of 244 °C with respect to LB-LA (ΔT= 120 °C). Although LB-LA (220) and LB-LA (220)-CNT liberate less hydrogen than LB-LA due to

complete decomposition of LiAlH$_4$ during sample preparation, faster dehydrogenation kinetics and significant reduction of onset dehydrogenation temperature of thermally stable LiBH$_4$ can be obtained. By ball milling of LB-LA (220), particle size reduction and good distribution of all phases (Figure 4.4B) result in de/rehydrogenation kinetic improvement (Choi, Lu, Sohn, and Fang, 2011). Moreover, good particle dispersion, especially Al in LiBH$_4$ matrix favors the formation of AlB$_2$ and other active species during dehydrogenation of LiBH$_4$. These active phases lead not only to sorption kinetic improvement of LiBH$_4$ (Figure 4.5) but also reversibility of LiAlH$_4$ and/or Li$_3$AlH$_6$.
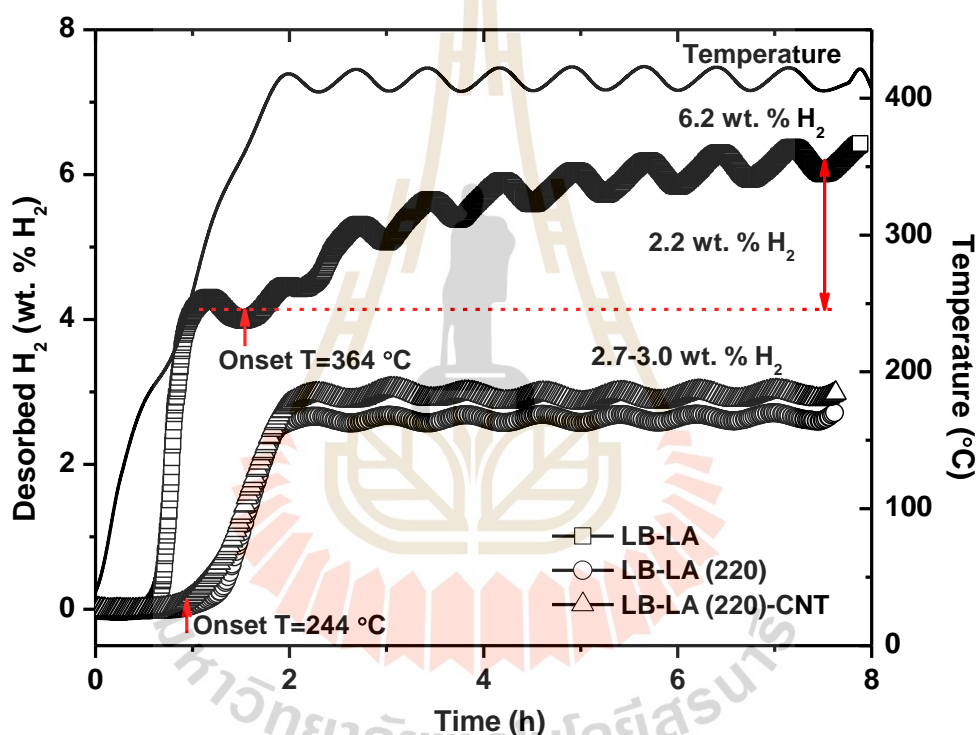
Figure 4.5 The 1st dehydrogenation kinetics of as-prepared LB-LA, LB-LA (220), and LB-LA (220)-CNT.

4.1.4 Reaction mechanisms

Reaction mechanisms during dehydrogenation of all samples are further characterized by PXD, FTIR, and solid-state ^{27}Al MAS NMR techniques. All dehydrogenated samples show comparable diffraction patterns of Al/LiH together with LiAlO$_2$ and Li$_2$O (LB-LA (220) and LB-LA (220)-CNT) due to oxidation of Li-containing phases and LiAl, respectively (Figure 4.6(b) and (c)). The FTIR spectra of all samples reveal vibrational peaks of B–H stretching and bending of LiBH$_4$ (2388-2226 and 1126 cm^{-1}, respectively), O–H bending of contamination

(1634 cm^{-1}), B–O asymmetric stretching due to oxidation of LiBH$_4$ and/ or amorphous B (1600-1300 cm^{-1}), and [B$_{12}$H$_{12}$]$^{2-}$ of Li$_2$B$_{12}$H$_{12}$ (2486 cm^{-1}) (Figure 4.7). The formation of Al/LiH, amorphous B, and Li$_2$B$_{12}$H$_{12}$ observed in dehydrogenated powder of LB-LA (Figure 4.6(a) and 4.7(a)) suggests individual decompositions of LiAlH$_4$ (equation (4.1) and (4.2)) and LiBH$_4$ (equation (4.3) and (4.4)). Moreover, the relative peak area of LiBH$_4$ vibrations (both stretching and bending at 2388-2226 and 1126 cm^{-1}, respectively) with respect to other phases in dehydrogenated LB-LA (220) and LB-LA (220)-CNT is significantly lower than that of LB-LA. This implies effective decomposition of thermally stable LiBH$_4$ in LB-LA (220) and LB-LA (220)-CNT, corresponding to superior kinetics and hydrogen content released from LB-LA (220) and LB-LA (220)-CNT compared to LB-LA (Figure 4.5).

$$LiBH_4(l) \longrightarrow LiH(s) + B(s) + 3/2H_2(g) \tag{4.3}$$

$$LiBH_4(l) \longrightarrow 1/12Li_2B_{12}H_{12}(s) + 5/6LiH(s) + 13/12H_2(g) \tag{4.4}$$

$$2LiBH_4(l) + Al(s) \longrightarrow 2LiH(s) + AlB_2(s) + 3H_2(g) \tag{4.5}$$

$$2LiH(s) + 2Al(s) \longrightarrow 2LiAl(s) + H_2(g) \tag{4.6}$$
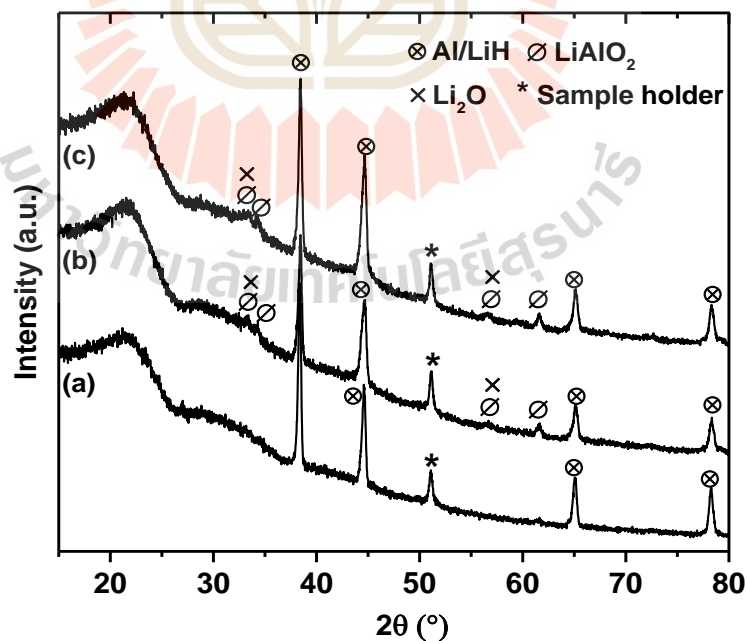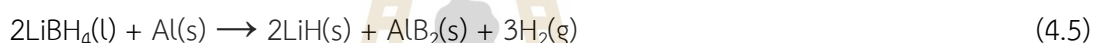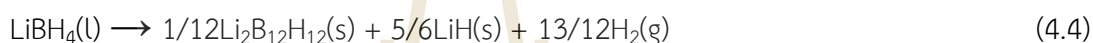

Figure 4.6 PXD spectra of dehydrogenated LB-LA (a), LB-LA (220) (b), and LB-LA (220)-CNT (c).
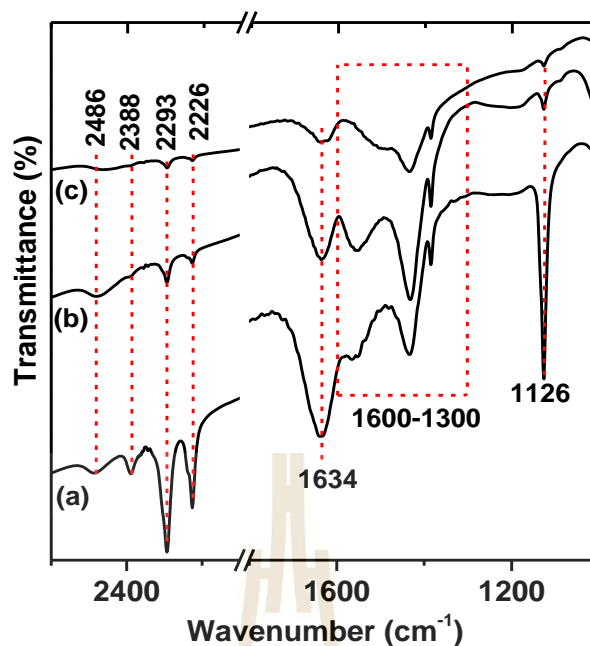
Figure 4.7 FTIR spectra of dehydrogenated LB-LA (a), LB-LA (220) (b), and LB-LA (220)-CNT (c).

In addition, Al-containing phases in dehydrogenated LB-LA (220) and LB-LA (220)-CNT are investigated by solid-state ^{27}Al MAS NMR technique. Both samples reveal characteristic peaks of metallic Al (1638 ppm) and doublet of β-LiAlO$_2$ (13 and 80 ppm) (Figure 4.8), approaching values in previous reports of 1640 ppm and doublet at 11.9 and 77.7 ppm for Al and β-LiAlO$_2$, respectively (Soru et al., 2014; Choi et al., 2011). Moreover, the resonance peaks of AlB$_2$ and β-LiAl (or γ-[Li$_3$Al$_3$]) at 865 and 393 ppm, respectively (Soru et al., 2014; Choi et al., 2011), are observed in LB-LA (220) (Figure 4.8(a)). The formation of AlB$_2$ is due to dehydrogenation of LiBH$_4$ via reacting with Al (equation (4.5)), while that of LiAl is from reaction between LiH and Al (equation (4.6)) (Choi et al., 2011).

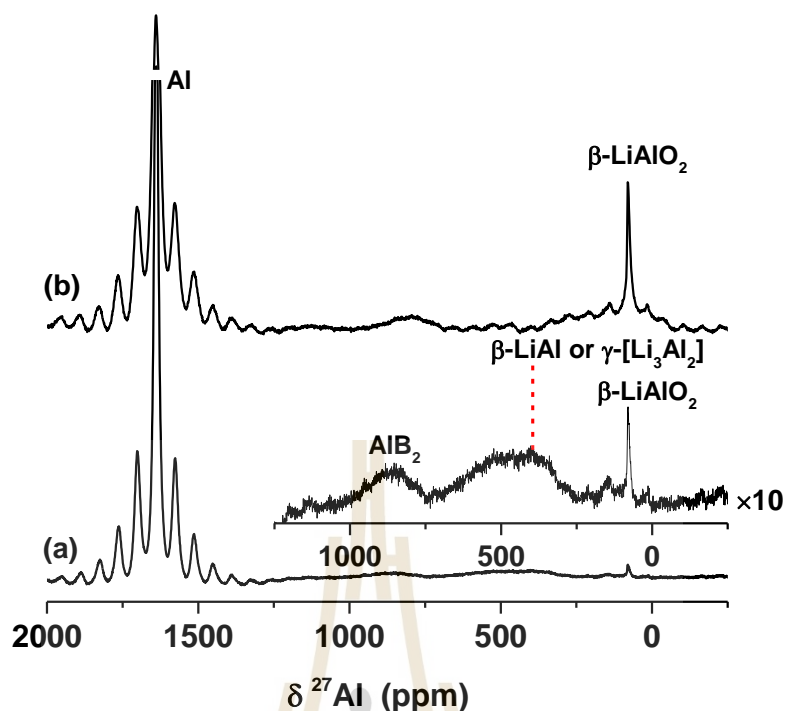**Figure 4.8** Solid-state ^{27}Al MAS NMR spectra of dehydrogenated LB-LA (220) (a) and LB-LA (220)-CNT (b).

Considering phase composition in dehydrogenated products, several step decompositions of LB-LA (220) and LB-LA (220)-CNT are summarized as follows. Both samples start with complete dehydrogenation of LiAlH$_4$ to produce LiH and Al (equation (4.1) and (4.2)) and melting of LiBH$_4$. Afterward, molten LiBH$_4$ proceeds by different mechanisms of (i) individual decomposition to LiH with either amorphous B (equation (4.3)) or Li$_2$B$_{12}$H$_{12}$ (equation (4.4)) and (ii) reaction with Al to form LiH and AlB$_2$ (equation (4.5)) (only LB-LA (220)). The LiH further reacts with Al to produce LiAl, which is possible at T >400 °C under low hydrogen pressure (equation (4.6)) (Liu et al., 2016; Meggouh, Grant and Walker, 2011; Choi et al., 2011). The formations AlB$_2$ and LiAl in dehydrogenated LB-LA (220), benefiting reversibility of LiBH$_4$ and LiAlH$_4$ (Liu et al., 2016; Hansen et al., 2013) can be achieved due to enhanced surface interaction between Al with molten LiBH$_4$ and LiH obtained from particle size reduction via ball milling. In the case of LB-LA (220)-CNT, the disappearance of AlB$_2$ might be due to the fact that dispersed MWCNTs in hydride matrices prevent contact between molten LiBH$_4$ and metallic Al.

4.1.5 Dehydrogenation kinetics and reversibility

Furthermore, dehydrogenation kinetics and reversibility of LB-LA, LB-LA (220), and LB-LA (220)-CNT (T= 400 °C and p(H$_2$)= 7 mbar) are characterized by titration measurements.

Hydrogen content produced from LB-LA during the 2nd cycle is 2.3 wt. % H_2 (Figure 4.9). For modified samples, LB-LA (220) releases comparable hydrogen content in the range of 2.5-2.8 wt. % H_2 within 3 h for three de/rehydrogenation cycles, while LB-LA (220)-CNT liberates 2.0-3.0 wt. % H_2 within 3-5 h (Figure 4.9). During the 1st cycle, LB-LA (220) and LB-LA (220)-CNT reveal comparable onset dehydrogenation temperatures of 246 °C, corresponding to decomposition of $LiBH_4$. During the 2nd and 3rd cycles, LB-LA (220) shows two-step decomposition at onset temperatures of 160 and 318 °C with storage capacities of ~0.5 and 2.0 wt. % H_2, respectively (Figure 4.9A), corresponding to dehydrogenation of $LiAlH_4$ (and/or Li_3AlH_6) and $LiBH_4$. For LB-LA and LB-LA (220)-CNT, only decomposition of $LiBH_4$ (2.0-2.3 wt. % H_2) is detected at a comparable onset temperature of 318 °C (Figure 4.9B). Thus, $LiAlH_4$ (and/or Li_3AlH_6) and $LiBH_4$ can be reproduced after rehydrogenation of LB-LA (220), whereas LB-LA and LB-LA (220)-CNT show recovery of only $LiBH_4$.
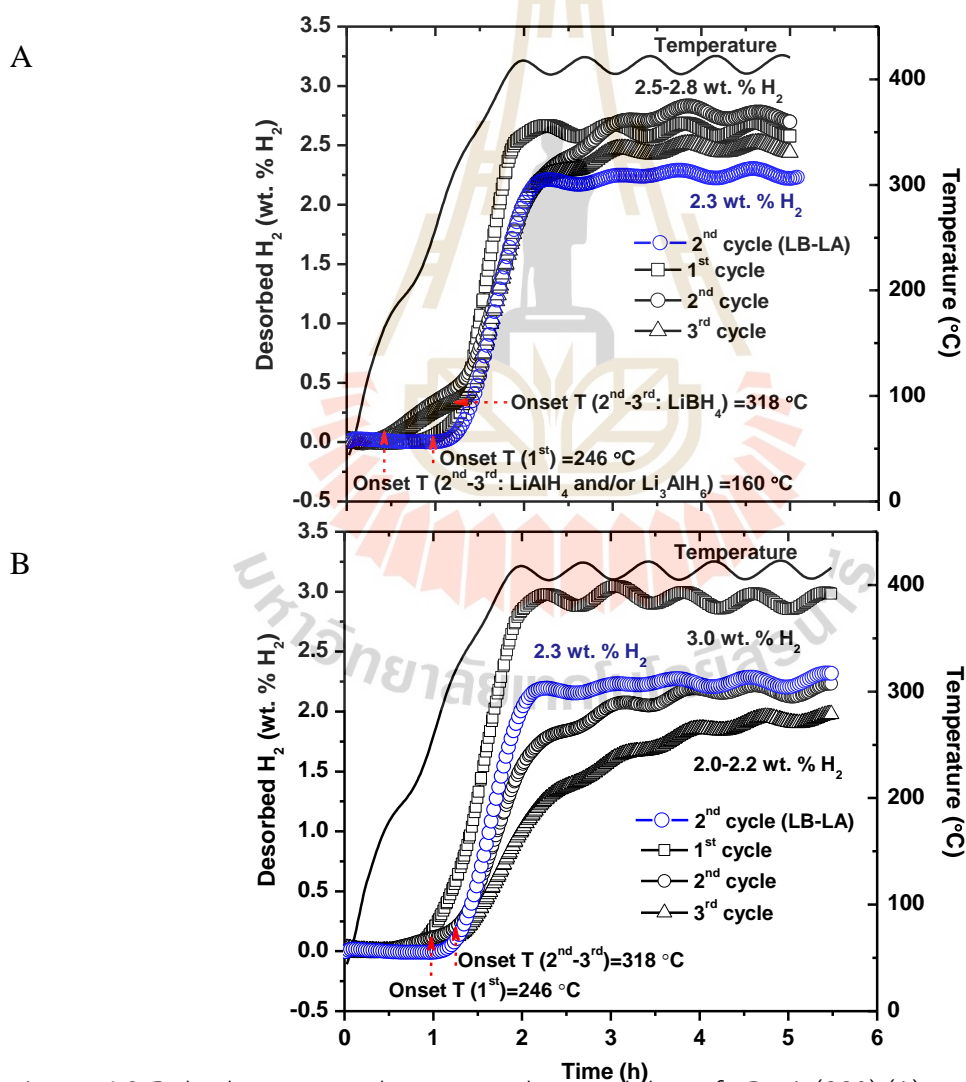

Figure 4.9 Dehydrogenation kinetics and reversibility of LB-LA (220) (A) and LB-LA (220)-CNT (B) with respect to LB-LA.

To further confirm the reversibility of hydride composite, chemical compositions in rehydrogenated LB-LA (220) and LB-LA (220)-CNT are characterized by PXD, FTIR, and ^{27}Al MAS NMR techniques. Comparable diffraction peaks of Al/LiH and Li_2O observed in rehydrogenated LB-LA (220) and LB-LA (220)-CNT indicate incomplete reversibility of $LiAlH_4$ and oxidation of Li-containing phases, respectively (Figure 4.10).In the case of FTIR results, rehydrogenated LB-LA (220) and LB-LA (220)-CNT reveal strong B–H vibrations of $LiBH_4$ (2388-2226 and 1128 cm^{-1} for stretching and bending, respectively) with respect to other phases (Figure 4.11), suggesting reversibility of $LiBH_4$. However, the clear vibrational peak of $Li_2B_{12}H_{12}$ at 2482 cm^{-1} hints at irreversibility of this thermally stable phase, corresponding to deficient hydrogen content released from the decomposition of $LiBH_4$ during the 2nd-3rd cycles (onset at 318 °C) (Figure 4.9).
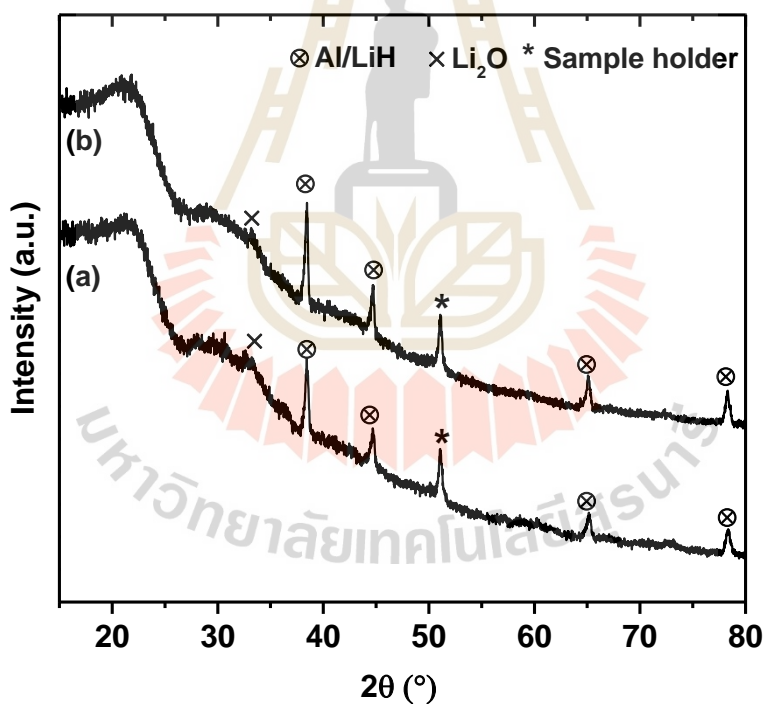

Figure 4.10 PXD spectra of rehydrogenated LB-LA (220) (a) and LB-LA (220)-CNT (b).
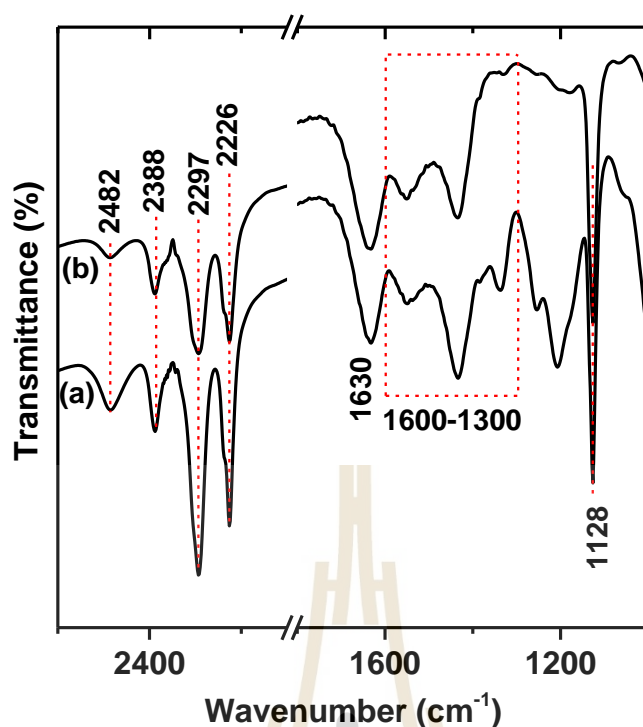
Figure 4.11 FTIR spectra of rehydrogenated LB-LA (220) (a) and LB-LA (220)-CNT (b).

For ^{27}Al MAS NMR spectra (Figure 4.12), rehydrogenated LB-LA (220) and LB-LA (220)-CNT show comparable characteristic peaks of metallic Al at 1640 ppm as well as α- and β-LiAlO$_2$ at 16.2 and 83.4 ppm, respectively (Choi et al., 2011). Moreover, the ^{27}Al MAS NMR spectrum of rehydrogenated LB-LA (220) exhibits the signals of LiAlH$_4$ and Li$_3$AlH$_6$ at 108.3 and -31.2 ppm, respectively (Figure 4.12(a)), while that of rehydrogenated LB-LA (220)-CNT reveals the chemical shift of six-coordinated oxidized Al^{III} derivatives (Al$_o$) at 65 ppm from the reaction of highly reactive Al and oxygen impurities (Figure 4.12(b)) (Wiench, Balema, Pecharsky, and Pruski, 2004). The reversibility of LiAlH$_4$ and Li$_3$AlH$_6$ after rehydrogenation of LB-LA (220) is consistent with the dehydrogenation at low onset temperature (160 °C) detected in the 2nd cycle (Figure 4.9A). Considering dehydrogenation kinetics and reversibility of LB-LA (220) and LB-LA (220)-CNT (Figure 4.9), reversibility of LiBH$_4$ in the 2nd and 3rd cycles is comparable (hydrogen content released of ~2.0-2.3 wt. % H$_2$ for both samples). Although the formation of AlB$_2$, favoring reversibility of LiBH$_4$ via reverse reaction of equation (4.6), cannot be achieved after dehydrogenation of LB-LA (220)-CNT, catalytic effects as well as enhanced hydrogen diffusion and thermal conductivity of carbon materials (MWCNTs in this study) (Ruffieux, Gr€oning, O., Bielmann, and Gr€oning, P., 2004; Adelhelm, and Jongh, 2011; Praphatsorn Plerdsranoy, Songwuit Chanthee, and Rapee Utke, 2017) benefit the reproducibility of LiBH$_4$. For LB-LA (220), the simple approach of reducing

particle size of Al obtained after decomposition of LiAlH$_4$ via ball milling encourages the formation of AlB$_2$ and LiAl. The latter leads to effective reversibility of LiBH$_4$, LiAlH$_4$, and Li$_3$AlH$_6$, and enhances hydrogen content desorbed upon cycling. Nevertheless, irreversible phases of metallic Al and Li$_2$B$_{12}$H$_{12}$ lead to lower hydrogen contents released and reproduced by both LB-LA (220) and LB-LA (220)-CNT.
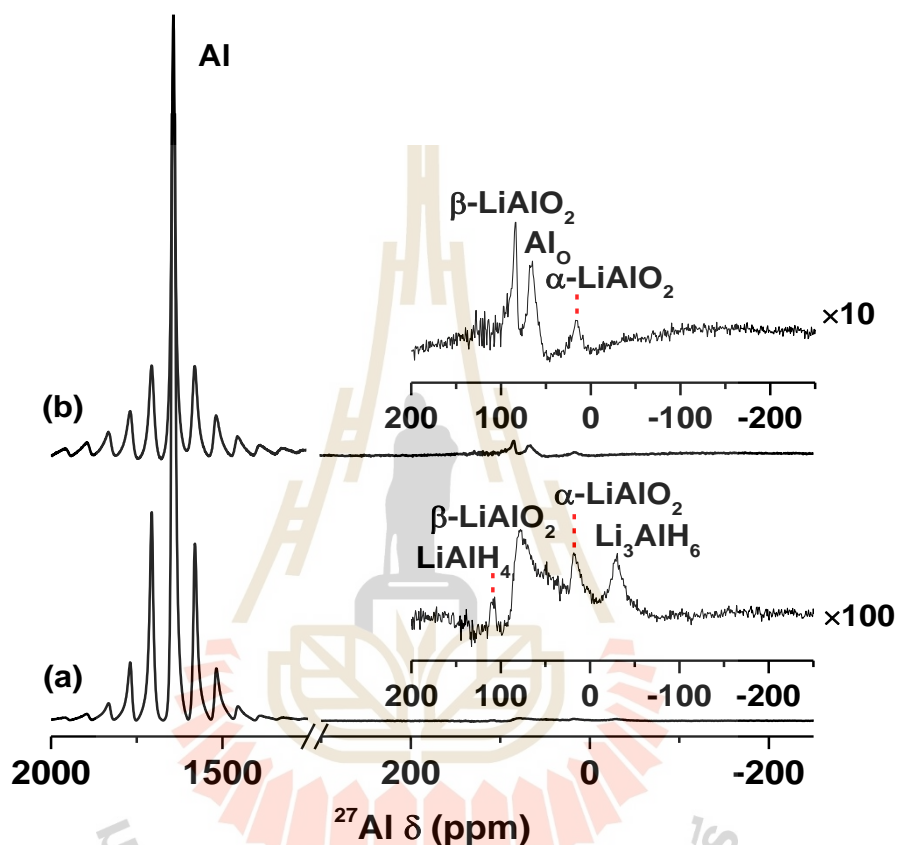

Figure 4.12 Solid-state 27Al MAS NMR spectra of rehydrogenated LB-LA (220) (a) and LB-LA (220)-CNT (b).

4.2   References

Adelhelm, P., and de Jongh, P. E. (2011). The impact of carbon materials on the hydrogen storage properties of light metal hydrides. *J. Mater Chem., 21,* 2417-2427.

B€osenberg, U., Ravnsbæk, D. B., Hagemann, H., D'Anna, V., Bonatto Minella, C., Pistidda, C., and Dornheim, M. (2010). Pressure and temperature influence on the desorption pathway of the $LiBH_4$-MgH_2 composite system. *J. Phys. Chem. C., 114*, 15212–15217.

Choi, Y. J., Lu, J., Sohn, H. Y., and Fang, Z. Z. (2011). Reaction mechanisms in the Li_3AlH_6/$LiBH_4$ and Al/$LiBH_4$ systems for reversible hydrogen storage. Part 1: H capacity and role of Al. *J. Phys. Chem. C., 115,* 6040–6047.

Choi, Y. J., Lu, L., Sohn, H. Y., Fang, Z. Z., Kim, C., Bowman Jr. R. C., and Hwang, S. J. (2011). Reaction mechanisms in the Li_3AlH_6/$LiBH_4$ and Al/$LiBH_4$ systems for reversible hydrogen storage. Part 2: solid-state NMR studied. *J. Phys. Chem. C., 115,* 6048–6056.

Deprez, E., Munoz-Maaquez, M. A., Jimenez de Haro, M. C., Palomares, F. J., Sorai, F., Dornheim, M., and Fernaandez, A. (2011). Combined X-ray photoelectron spectroscopy and scanning electron microscopy studies of the $LiBH_4$-MgH_2 reactive hydride composite with and without a Ti-based additive. *J. Appl. Phys., 109,* 014913.

Gosalawit-Utke, R., Meethom, S., Pistidda, C., Milanese, C., Laipple, D., Saisopa, T., and Dornheim, M. (2014). Destabilization of $LiBH_4$ by nanoconfinement in PMMA-co-BM polymer matrix for reversible hydrogen storage. *Int. J. Hydrogen Energy., 39,* 5019–5029.

Hansen, B. R. S., Ravnsbæk, D. B., Reed, D., Book, D., Gundlach, C., Skibsted, J., and Jensen, T. R. (2013). Hydrogen storage capacity loss in a $LiBH_4$-Al composite. *J. Phys. Chem. C., 117,* 7423–7432.

Kamitsos, E. I., Karakassides, M. A., and Chryssikos, G. D. (1987). Vibrational spectra of magnesium-sodium-borate glasses. 2. Raman and mid-infrared investigation of the network structure. *J. Phys. Chem., 91,* 1073–1079.

Liu, H., Wang, X., Zhou, H., Gao, S., Ge, H., Li, S., and Yan, M. (2016). Improved hydrogen desorption properties of $LiBH_4$ by AlH_3 addition. *Int. J. Hydrogen Energy., 41,* 22118–22127.

Meggouh, M., Grant, D. M., and Walker, G. S. (2011). Optimizing the destabilization of $LiBH_4$ for hydrogen storage and the effect of different Al sources. *J. Phys. Chem. C., 115,* 22054–22061.

Plerdsranoy, P., and Utke, R. (2015). Confined LiBH$_4$-LiAlH$_4$ in nanopores of activated carbon nanofibers. *Int. J. Hydrogen Energy., 40,* 7083–7092.

Plerdsranoy, P. Chanthee, S., and Utke., R. (2017). Compaction of LiBH$_4$-MgH$_2$ doped with MWCNTs-TiO$_2$ for reversible hydrogen storage. *Int. J. Hydrogen Energy., 42,* 978–986.

Ruffieux, P., Gr€oning, O., Bielmann, M., and Gr€oning, P. (2004). Hydrogen chemisorption on sp^2- bonded carbon: influence of the local curvature and local electronic effects. *Appl. Phys. A., 78,* 975–980.

Soru, S., Taras, A., Pistidda, C., Milanese, C., Bonatto Minella, C., Masolo, E., and Garroni, S. (2014). Structural evolution upon decomposition of the LiAlH$_4$-LiBH$_4$ system. *J. Alloy. Comp., 615,* S693–S697.

Thiangviriya, S., and Utke, R. (2016). Improvement of dehydrogenation kinetics of 2LiBH$_4$-MgH$_2$ composite by doping with activated carbon nanofibers. *Int. J. Hydrogen Energy., 41,* 2797–2806.

U.S. Department of Commerce. (2012). *National Institute of Standards and Technology (NIST): NIST Inorganic Crystal Structure Database (ICSD) SRD 3.* Retrieved from https://srdata.nist.gov/xps/main_search_menu.aspx

Wiench, J. W., Balema, V. P., Pecharsky, V. K., and Pruski, M. (2017). Solid-state ^{27}Al NMR investigation of thermal decomposition of LiAlH$_4$. *J. Solid State Chem., 177,* 648–653.

Zhao, Y., Liu, H., Liu, Y., Wang, Y., Yuan, H., and Jiao, L. (2017). Synergistic effects of destabilization, catalysis and nanoconfinement on dehydrogenation of LiBH$_4$. *Int. J. Hydrogen Energy., 42,* 1354–1360.

CHAPTER V

CONCLUSIONS

In this thesis, reversibility of $LiBH_4$ and $LiAlH_4$ (or Li_3AlH_6) in LB-LA composite was improved by ball milling of dehydrogenated LB-LA quenched at 220 °C (LB-LA (220)). This resulted in particle size reduction and good dispersion of all species, especially metallic Al and effective formation of AlB_2 and LiAl upon dehydrogenation. In addition, MWCNTs enhancing hydrogen diffusion and thermal conductivity for de/rehydrogenation were doped into LB-LA (220) to obtain LB-LA (220)-CNT. The LB-LA showed two-step decomposition of $LiAlH_4$ and $LiBH_4$ together with storage capacities of ~4.0 and 2.2 wt. % H_2, respectively, while LB-LA (220) and LB-LA (220)-CNT revealed only decomposition of $LiBH_4$ with 2.7-3.0 wt. % H_2. With respect to LB-LA, reduction of onset temperature (ΔT= 120 °C) and rapid kinetics (~three times) during dehydrogenation of the thermally stable phase of $LiBH_4$ were observed for LB-LA (220) and LB-LA (220)-CNT. Dehydrogenation of LB-LA proceeded through individual reactions of $LiAlH_4$ and $LiBH_4$ to produce Al, LiH, amorphous B, and $Li_2B_{12}H_{12}$ without any active species. For LB-LA (220) and LB-LA (220)-CNT, in addition to comparable phases with LBLA, the formation of AlB_2 (only LB-LA (220)) and LiAl suggested effective reaction of Al with molten $LiBH_4$ and LiH, respectively, due to high surface area and good distribution of Al. Owing to the formation of AlB_2 and LiAl, reversibility of $LiBH_4$, $LiAlH_4$, and Li_3AlH_6 was found in LB-LA (220), but LB-LA (220)-CNT showed only reversibility of $LiBH_4$. This might be explained by the fact that contact between Al and other phases was obstructed by dispersion of MWCNTs in hydride matrices, leading to deficient formation of active species for reversibility.

CURRICULUM VITAE

Name   Miss Sukanya Meethom

Date of Birth   December 26th 1987

Place of Birth   Nakhon Ratchasima, Thailand

Educations (Years, Degrees, Majors, and Universities)

        2006-2009   Bachelor of Science (Chemistry), Rajamankala University of Technology Isan, Nakhon Ratchasima Campus, Thailand

        2010-2013   Master of Science (Biochemistry), Suranaree University of Technology, Thailand

        2014-2022   Doctor of Philosophy (Chemistry), Suranaree University of Technology, Thailand

Publications

Sitthiwet, C., Thiangviriya, S., Thaweelap, N., **Meethom**, **S.,** Kaewsuwan, D., Chanlek, N., and Utke, R. (2017). Hydrogen sorption and permeability of compacted $LiBH_4$ nanoconfined into activated carbon nanofibers impregnated with TiO_2. *Journal of Physics and Chemistry of Solids. 110,* 344-353.

Meethom, **S.,** Kaewsuwan, D., Chanlek, N., Utke, O., and Utke, R. (2020). Enhanced hydrogen sorption of $LiBH_4$–$LiAlH_4$ by quenching dehydrogenation, ball milling, and doping with MWCNTs. *Journal of Physics and Chemistry of Solids. 136,* 10920-10926.

Grants and Fellowships - Science Achievement Scholarship of Thailand (SAST-002/2558)

        - Thailand Research Fund and Suranaree University (TRF)

        - Research Network NANOTEC (RNN) program of the National Nanotechnology Center (NANOTEC)

        - National Science and Technology Development Agency (NSTDA)

        - Ministry of Science and Technology, Thailand